Title

Promotion of cholangiocarcinoma growth by diverse cancer-associated fibroblast subpopulations

Journal

Cancer Cell, 39(6)

ISSN

1535-6108

Authors

Affo, Silvia
Nair, Ajay
Brundu, Francesco
et al.

Publication Date

2021-06-01

DOI

10.1016/j.ccell.2021.03.012

Peer reviewed

HHS Public Access

Author manuscript

Cancer Cell. Author manuscript; available in PMC 2022 June 14.

Published in final edited form as:

Cancer Cell. 2021 June 14; 39(6): 866–882.e11. doi:10.1016/j.ccell.2021.03.012.

Promotion of Cholangiocarcinoma Growth by Diverse Cancer-associated Fibroblast Subpopulations

Silvia Affo[1], **Ajay Nair**[#2], **Francesco Brundu**[#2], **Aashreya Ravichandra**[#1], **Sonakshi Bhattacharjee**[1], **Michitaka Matsuda**[3], **LiKang Chin**[4], **Aveline Filliol**[1], **Wen Wen**[1], **Xinhua Song**[5], **Aubrianna Decker**[6], **Jeremy Worley**[2], **Jorge Matias Caviglia**[1], **Lexing Yu**[1], **Deqi Yin**[1], **Yoshinobu Saito**[1], **Thomas Savage**[7], **Rebecca G. Wells**[4], **Matthias Mack**[8], **Lars Zender**[9,10,11], **Nicholas Arpaia**[7,12], **Helen E. Remotti**[13], **Raul Rabadan**[2], **Peter Sims**[14], **Anne-Laure Leblond**[15], **Achim Weber**[15], **Marc-Oliver Riener**[15], **Brent R. Stockwell**[6,16], **Jellert Gaublomme**[6], **Josep M. Llovet**[17,18,19], **Raghu Kalluri**[24], **George K. Michalopoulos**[20], **Ekihiro Seki**[3], **Daniela Sia**[18], **Xin Chen**[5], **Andrea Califano**[2,12,14,21,22], **Robert F. Schwabe**[*,1,12,23]

[1]Department of Medicine, Columbia University, New York, 10032, NY, USA. [2]Department of Systems Biology, Columbia University Irving Medical Center, New York, 10032, NY, USA. [3]Department of Medicine, Division of Digestive and Liver Diseases, Cedars-Sinai Medical Center, Los Angeles, 90024, CA, USA. [4]Department of Medicine, Penn Physical Sciences in Oncology Center PSOC@Penn, University of Pennsylvania, Philadelphia, PA 19104, USA [5]Department of Bioengineering and Therapeutic Sciences and Liver Center, University of California, San Francisco, 94158, CA, USA. [6]Department of Biological Sciences, Columbia University, New York, 10027, NY, USA. [7]Department of Microbiology and Immunology, Vagelos College of Physicians and Surgeons, Columbia University, New York, 10032, NY, USA. [8]Department of Nephrology, University Hospital Regensburg, 93053, Regensburg, Germany. [9]Department of Medical Oncology and Pneumology, University Hospital Tuebingen, 72076, Tuebingen, Germany. [10]German Cancer Research Consortium (DKTK), German Cancer Research Center (DKFZ), 69120, Heidelberg, Germany. [11]iFIT Cluster of Excellence EXC 2180, University of Tuebingen, 72076, Tuebingen, Germany. [12]Herbert Irving Comprehensive Cancer Center, Columbia University, New York, 10032, NY, USA. [13]Department of Pathology & Cell Biology, Columbia University, New York, 10032, NY, USA. [14]Department of Systems Biology, Columbia University, New York, 10032, NY, USA. [15]Department for Pathology and Molecular Pathology, Zürich University Hospital, 8091, Zürich, Switzerland. [16]Department of Chemistry, Columbia University,

[*]Lead Contact and Corresponding Author: Robert F. Schwabe (rfs2102@cumc.columbia.edu).

AUTHOR CONTRIBUTIONS

Conceptualization, R.F.S and S.A.; Methodology, R.F.S., S.A., X.C., R.G.W., A.N., F.B., D.S.; Experimentation, S.A., A.N, F.B., A.R., S.B., T.S., M.M., L.C., A.F., W.W., Y.S., J.W., D.Y., X.S., A.D., J.M.C., L.Z., H.E.R., A.L.L., D.S.; Writing, R.F.S and S.A.; Funding Acquisition, R.F.S., X.C. and S.A.; Resources, R.F.S., N.A., A.M., M.O.R., B.R.S., J.G., G.K.M., L.S., J.M.L., D.S., E.S., R.R., P.S., X.C., and A.C.; Supervision, R.F.S.

DECLARATION OF INTERESTS

Dr. Califano is founder, equity holder, consultant, and director of DarwinHealth Inc. Columbia University is an equity holder in DarwinHealth Inc.

New York, 10027, NY, USA [17]Liver Cancer Translational Research Laboratory, Institut d'Investigacions Biomèdiques August Pi i Sunyer, Hospital Clínic, Universitat de Barcelona, 08036, Barcelona, Spain. [18]Mount Sinai Liver Cancer Program, Divisions of Liver Diseases, Tisch Cancer Institute, Icahn School of Medicine at Mount Sinai, New York, 10029, NY, USA. [19]Institució Catalana de Recerca i Estudis Avançats, Barcelona, Spain. [20]Department of Pathology, University of Pittsburgh, Pittsburgh, 15213, PA, USA. [21]Department of Biomedical Informatics, Columbia University, New York, 10032, NY, USA. [22]Department of Biochemistry & Molecular Biophysics, Columbia University, New York, 10032, NY, USA. [23]Institute of Human Nutrition, Columbia University, New York, 10032, NY, USA. [24]Department of Cancer Biology, Metastasis Research Center, University of Texas MD Anderson Cancer Center, Houston, TX 77030, USA

[#] These authors contributed equally to this work.

SUMMARY

Cancer-associated fibroblasts (CAF) are a poorly characterized cell population in the context of liver cancer. Our study investigates CAF functions in intrahepatic cholangiocarcinoma (ICC), a highly desmoplastic liver tumor. Genetic tracing, single-cell RNA-sequencing and ligand-receptor analyses uncovered hepatic stellate cells (HSC) as the main source of CAF, and HSC-derived CAF as dominant population interacting with tumor cells. In mice, CAF promotes ICC progression, as revealed by HSC-selective CAF depletion. In patients, a high panCAF signature is associated with decreased survival and increased recurrence. Single-cell RNA-sequencing segregates CAF into inflammatory and growth factor-enriched (iCAF) and myofibroblastic (myCAF) subpopulations, displaying distinct ligand-receptor interactions. myCAF-expressed hyaluronan synthase 2 but not type I collagen, promotes ICC. iCAF-expressed HGF enhances ICC growth via tumor-expressed MET, thus directly linking CAF to tumor cells. In summary, our data demonstrate promotion of desmoplastic ICC growth by therapeutically targetable CAF subtype-specific mediators, but not by type I collagen.

eTOC blurb

Intrahepatic cholangiocarcinoma (ICC) is an extraordinarily stiff liver tumor due to abundant scar-forming cancer-associated fibroblasts (CAF). Here, Affo et al. determine origin and functions of CAF, and uncover distinct CAF subsets, promoting ICC growth via different therapeutically targetable mediators. Thus, CAF and their mediators may serve as therapeutic targets for ICC.

Graphical Abstract

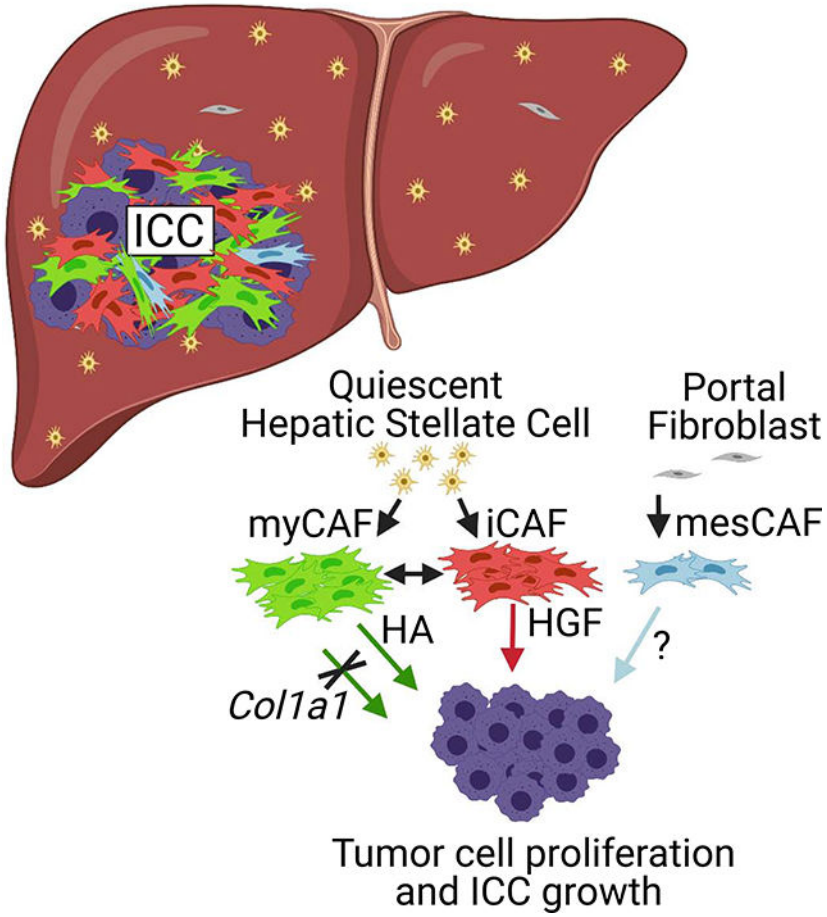

Keywords

Tumor microenvironment; cholangiocarcinoma; YAP; KRAS; single-cell; CellphoneDB; stiffness

INTRODUCTION

Cancer-associated fibroblasts (CAF) are an abundant but insufficiently characterized cell type in the tumor microenvironment (TME) that may promote or restrain tumor growth in a context- and organ-specific manner (Biffi and Tuveson, 2020; Erez et al., 2010; Kalluri, 2016; Ozdemir et al., 2014; Rhim et al., 2014; Sahai et al., 2020; Su et al., 2018). The mechanisms underlying CAF-mediated tumor promotion or restriction remain incompletely understood. Recent studies have revealed CAF diversity by transcriptomics (Biffi and Tuveson, 2020; Chen and Song, 2019; Costa et al., 2018; Elyada et al., 2019; Ohlund et al., 2017; Su et al., 2018; Zhang et al., 2020a). As additional contributor to diversity, CAF may arise from different cellular sources including resident fibroblasts, pericytes, mesenchymal stem cells, bone marrow, and adipocytes (Biffi and Tuveson, 2020; Chen and Song, 2019; Sahai et al., 2020). However, the in vivo role of CAF subpopulations and associated mediators remain largely elusive. Moreover, many insights on CAF are derived from

genetically engineered mouse models of pancreatic ductal adenocarcinoma (PDAC) and breast cancer, with only a few studies in other organs including the liver.

Cholangiocarcinoma (CCA), the second most common primary malignancy of the liver, is a desmoplastic tumor with abundant CAF, few therapeutic options, and dismal prognosis (Banales et al., 2020; Rizvi et al., 2018b). The increased incidence of CCA is largely due to a rise in intrahepatic CCA (ICC) (Banales et al., 2020), possibly due to increased non-alcoholic fatty liver disease (Banales et al., 2020; Clements et al., 2020). ICC shares anatomic, embryologic, and genetic features with PDAC. However, while the contribution of CAF to tumor growth has been the subject of numerous in vivo studies in PDAC, the functions of CAF in CCA have not been studied thoroughly in vivo. In PDAC, the restraint of tumor aggressiveness and progression by α-smooth muscle actin-positive (αSMA^{+}) CAF in vivo contrasts the tumor-promoting effects of CAF observed *in vitro*, emphasizing the importance of careful *in vivo* studies. Moreover, there is increased evidence for diverse functions of CAF subtypes, notably myofibroblastic (myCAF) and inflammatory CAF (iCAF) (Biffi and Tuveson, 2020), but *in vivo* functions of these CAF subpopulations and their mediators, in particular CAF-secreted extracellular matrix (ECM), remain largely elusive. While it is widely assumed that crosslinked type I collagen, promotes tumors *via* increased stiffness and mechanosensitive signaling (Barbazan and Matic Vignjevic, 2019; Levental et al., 2009; Northey et al., 2017), ECM can also provide a mechanical barrier restricting tumor spread (Egeblad et al., 2010; Liotta, 1986).

Insights on CAF functions in ICC are derived from *in vitro* studies (Affo et al., 2017; Sirica, 2011) and a single *in vivo* study using an orthotopic implantation model and BCL2-inhibitor navitoclax, which depletes CAF but may also affect tumor and hematopoietic cells (Mertens et al., 2013). In contrast to other organs, fibroblast ontogeny is well-defined in the liver, with hepatic stellate cells (HSC) contributing 85–95% of fibroblasts (Mederacke et al., 2013). Here, we took advantage of *Lrat*-Cre-transgenic mice (Mederacke et al., 2013) as powerful tool to trace and functionally manipulate this well-defined fibroblast precursor population, providing insights into CAF biology in ICC and the role of CAF-derived mediators in endogenously arising ICC models. Our study reveals HSC-derived CAF as the population that most intensely interacts with tumor cells, promoting ICC growth via CAF subtype-specific mediators but not type I collagen. Our data expand insights into pathways that drive the growth of this deadly tumor and challenge paradigms on collagen as central tumor-promoting mediator.

RESULTS

Hepatic stellate cell-derived CAF are the main tumor-interacting population in ICC

Hepatic overexpression of oncogenic driver $KRAS^{G12D}$ in combination with p19 CRISPR (KRAS/p19), or myr-AKT in combination with either YAP^{S127A} (YAP/AKT), NICD1 (NICD/AKT) or FBXW7Δf (FBXW7Δf/AKT) via the sleeping beauty system, delivered by hydrodynamic tail vein injection (Fan et al., 2012; Seehawer et al., 2018; Wang et al., 2019), resulted in the development of histopathologically confirmed cytokeratin 7 and 19-positive ICC. All tumors were desmoplastic, displaying high Acta2 and Col1a1 mRNA (Figures 1A, 1B) and abundant Col1a1-GFP and αSMA-positive CAF (Figures 1B, S1A, S1B). Using

Lrat-Cre-driven lox-stop-lox-TdTomato (TdTom) as a faithful strategy to label HSC (Mederacke et al., 2013), we observed that 85–95% of Col1a1-GFP$^+$ CAF and 85–93% of αSMA$^+$ CAF in these four desmoplastic ICC models were marked by Lrat-Cre-driven TdTom, suggesting HSC origin (Figures 1B, S1A, S1B). All subsequent studies, including single-cell RNA-sequencing (scRNA-seq), CAF depletion and HSC-selective knockouts were performed in two ICC models: YAP/AKT-induced ICC as most widely used AKT-driven ICC model, and KRAS/p19 incorporating KRAS^{G12D} as model incorporating a common mutation in ICC and leading to distinct tumor lesion, allowing for specific mechanistic studies such as rheometry (Table S1). Lrat-Cre tracing was confirmed by scRNA-seq in 4 murine ICC samples (n=3 YAP/AKT, n=1 KRAS/p19). 91.9±2.8% of panCAF, defined by a scRNA signature (Table S2), expressed a HSC signature, including Lrat, Desmin, Colec11 and Rgs5, whereas only 6.3±2.3% expressed Msln, Upk3b, Gpm6a, and Upk1b as markers of portal fibroblasts (PF), a second fibrogenic population in the liver with mesothelial characteristics (Figures 1C, S1C–J, Table S2). Comparison of HSC-CAF to fibrosis-associated HSC from biliary fibrosis, induced either by ligation of the common bile duct BDL) and three week diet containing 0.1% 3,5-diethoxycarbonyl-1,4-dihydrocollidine (DDC), revealed most genes and pathways as shared but uncovered higher activation in HSC-CAF (Figure 1D; Table S3), suggesting differentiation of HSC into highly activated HSC-CAF in the TME. To determine mechanisms through which HSC-CAF affect ICC, we analyzed ligand-receptor interactions by CellPhoneDB (Vento-Tormo et al., 2018). In murine scRNA-seq samples (n=4), CAF were the predominant cell population interacting with tumor cells, and among these, HSC-CAF represented the subpopulation with the most ligand-receptor interactions with tumor cells (Figures 1E, 1F, S1K–N). scRNA-seq analysis of human ICC (n=6) and hilar cholangiocarcinoma (CCA, n=1) samples confirmed the predominance of HSC-CAF (90.7±6.4% of all CAF in ICC, 100% in CCA), expressing *RGS5*, *LUM*, and *COLEC11*, and low abundance PF-CAF (9.3±6.4% of all CAF in ICC, not detected in CCA), expressing *MSLN* and *UPK1B* (Figures 1G, 1H, S1H, S1J, Table S1). Similar to mice, we found strong ligand-receptor interactions between panCAF and tumor cells, and between HSC-CAF and tumor cells in human ICC (n=5) and human CCA (n=1) (Figures 1G, 1H, S1M, S1N). Importantly, a high panCAF signature, developed from our scRNA-seq data, as well as high *ACTA2* mRNA expression, were associated with decreased survival and increased recurrence risk in ICC patients in the Sia (Sia et al., 2013) cohort (Figures 1I, Figure S1O; Table 1) as was high αSMA protein in tissue microarrays (TMA) from the Riener (Riener et al., 2010) cohort (Figure S1P). Moreover, a high panCAF signature was significantly enriched in the ICC proliferation subclass versus the inflammation subclass (Sia et al., 2013) and was associated with moderate to poor cell differentiation and intraneural invasion (Table 1). Together, these findings support our hypothesis that HSC-CAF modulate ICC biology and outcomes and suggest that this may be mediated through direct interactions with tumor cells.

To extend our findings beyond the liver, we analyzed scRNA-seq CAF data from KPC-induced PDAC and identified pancreatic stellate cells (PSC)-CAF and mesothelial CAF as main CAF populations (Figures 2A). PSC-CAF only weakly expressed HSC markers *Lrat*, *Des* or *Rgs5* (Figure 2B) but they shared most stellate cells (SC) genes in a global SC signature with HSC-CAF (Figures 2C, S2A–E). Similar to PF-CAF in ICC, mesothelial

CAF in PDAC highly expressed *Msln*, *Upk1b*, *Upk3b* and *Gpm6a* (Figure 2D). These data suggest similar CAF ontogeny in pancreas and liver, consistent with the finding that both organs contain stellate cells (Ohlund et al., 2017; Senoo et al., 2017).

HSC-derived CAF promote ICC growth

To elucidate CAF functions in ICC, we depleted HSC-CAF by crossing *Lrat*-Cre transgenic mice with lox-stop-lox-*Hbegf* (Cre-inducible diphtheria toxin receptor=iDTR transgenic mice); or depleted αSMA$^+$ CAF, representing the more myofibroblastic subpopulation of CAF (Biffi and Tuveson, 2020), as shown by colocalization of αSMA with *Col1a1*-GFP$^+$ or co-expression of *Acta2* with *Col1a1* mRNA in the HSC-CAF population (Figures S3A, S3B), via αSMA-driven thymidine kinase. Depletion by either strategy during the last two weeks of our tumor models reduced CAF by up to 85% with concomitantly reduced fibrosis (Figures 3A–C, S3C, S3D). Depleting CAF by either approach suppressed ICC development, evidenced by significant reductions of the liver-body ratio and CK19$^+$ tumor area (Figures 3A–C). In contrast, when CAF were depleted early, which led to a transient decrease but almost full recovery two weeks later, tumor growth was not affected (Figures S3E, S3F). As a complementary approach, we deleted *Pdgrfb* via *Lrat*-Cre, which decreased αSMA and fibrosis and also reduced ICC formation (Figures S3G, S3H). Next, we sought to understand how CAF promote ICC development. CAF-depleted mice displayed significantly reduced tumor cell proliferation, whereas apoptosis was unaltered or even reduced in tumors of CAF-depleted mice (Figures 3D, 3E, S3I). Consistent with the low immunogenicity of oncogene-driven tumors, we observed only few infiltrating CD3$^+$ T cells and no significant differences of lymphocyte and myeloid subsets between CAF-depleted and non-depleted mice (Figures 3F, S3J–M), with the exception of CD4$^+$FOXP3$^+$ Treg. The observed minor reduction of CD4$^+$FOXP3$^+$ Treg after CAF depletion (Figure 3F) is consistent with the ability of CAF to promote differentiation of T lymphocytes into Treg (Costa et al., 2018). Moreover, HSC promoted ICC growth when coinjected with tumor cells into *Rag2* knockout mice (Figure S3N), suggesting tumor promotion by direct HSC-CAF in the absence of adaptive immunity, in this subcutaneous model. As NF-κB regulates CAF-mediated inflammation and tumor growth in the skin (Erez et al., 2010), we studied its role in ICC. Deletion of NF-κB subunit *RelA* via *Lrat*-Cre was efficient but did not reduce ICC growth (Figures S3O, S3P). In summary, our studies suggest that direct CAF-tumor interactions trigger tumor cell proliferation and represent a major mechanism through which CAF may promote ICC growth, whereas modulation of cell death, adaptive immunity, or inflammation appear to only play minor roles in the investigated models.

CAF promote tumor growth independently of type I collagen

Next, we sought to uncover mediators through which HSC-derived CAF promote ICC growth. To test the hypothesis that CAF in ICC may be functionally diverse with distinct pathways and ligand-receptor interactomes, we analyzed murine and human CAF by scRNA-seq. By this approach, we uncovered subpopulations of inflammatory and growth factor-enriched CAF (iCAF), myofibroblastic CAF (myCAF) as well as CAF expressing PF/mesothelial markers, termed mesothelial CAF (mesCAF) (Figures 4A, S4A–D). Some CAF, fitting multiple categories, were denoted as “multi-CAF”, and few CAF, not fitting above categories, as “other CAF”. iCAF were part of the HSC cluster, expressing high levels of

quiescence markers *Lrat*, *Reln*, and *Rgs5,* and low activation markers *Col1a1*, *Acta2*, *Col8a1*, *Col15a1*, *Crlf1* and *Fbn2* (Figures 4A, S4A, S4B), and were enriched for inflammatory, growth factors and antigen presentation genes as well as receptor-ligand, growth factor and cytokine activity pathways (Figures 4A, S4A, S4B Table S4). myCAF were also part of the HSC-CAF cluster, but expressing lower HSC quiescence and higher activation markers than iCAF (Figures 4A, S4A–D) and enriched for ECM pathways (Table S5). Using *Rgs5* as marker for the iCAF population and *Col1a1*-GFP and SERPINF1 as markers for myCAF, we confirmed these *in situ* as separate populations of TdTom $^{+}$*Rgs5*^{high}*Col1a1*-GFP^{low} HSC-CAF, reminiscent of iCAF; and TdTom^{+}*Rgs5*^{low}*Col1a1*-GFP^{high} HSC-CAF, reminiscent of myCAF, in both murine ICC models (Figure 4B); and high RGS5 and low SERPINF1 (resembling iCAF) and low RGS5 and high SERPINF1 (resembling myCAF) CAF in human ICC (Figure 4C). However, there appeared to be no specific spatial distribution of iCAF and myCAF in murine or human ICC. myCAF and iCAF strongly interacted with tumor cells in CellPhoneDB ligand-receptor analysis in murine ICC (Figures 4D, S4E) and in human ICC and CCA (Figures 4D, S4F). myCAF represented 32.5±4.6% of CAF in murine ICC, 26.2±3.9% of CAF in human ICC (Figure 4A), and 66.8% in human CCA. Notably, high expression of the scRNA-seq-derived myCAF signature was associated with decreased survival (Figure 5A) and showed a trend towards higher recurrence in the Sia cohort (Sia et al., 2013) (Figure S4G). The myCAF signature was enriched in the ICC proliferation subclass versus the inflammation subclass and associated with intraneural invasion (Table 1). There were also differences in the myCAF signature in regards to racial background but subgroups were too small for meaningful subgroup analysis. As desmoplasia, collagen content and stiffness are closely intertwined and thought to impact on tumor growth *via* mechanosensitive signals (Barbazan and Matic Vignjevic, 2019; Levental et al., 2009; Northey et al., 2017), we first focus on type I collagen as tumor-modulating myCAF candidate mediator in ICC. *Col1a1* was strongly upregulated in murine and human ICC, and increased in CAF versus quiescent HSC (Figures 1A, 5B). ScRNA-seq and CellPhoneDB analysis revealed that *Col1a1* was enriched in myCAF, while a cognate receptor, *DDR1*, was expressed in tumor cells (Figures 5C, 5D), suggesting COL1A1-DDR1 as link between myCAF and tumor cells besides pure collagen-mediated mechanosensitive signals. Deletion of *Col1a1* from HSC via *Lrat*-Cre was highly efficient in KRAS/p19- and YAP/AKT-induced ICC (Figure 5E) and was accompanied by decreased tumor stiffness and decreased expression of YAP, a mechanosensitive transcriptional co-activator with key roles in CCA (Marti et al., 2015) (Figures 5F, S5A). Along this line, culturing ICC cells on stiff surfaces, increased proliferation of human ICC line HuCCT-1 (Figure S5B). However, despite reduced stiffness and decreased mechanosensitive signals, *Col1a1* deletion in HSC-CAF did not inhibit tumor growth in either ICC model (Figures 5G, 5H). As additional approach, we deleted type I collagen in all liver cells *via Mx1*-Cre. Deletion of *Col1a1 via Mx1*-Cre at different time points was also highly efficient but again did not reduce tumor growth while reducing stiffness (Figures S5C–G). Conditional deletion of above-discussed collagen receptor *Ddr*1 (Figure S5H), which was highly increased in human and mouse ICC (Figures 5I, S5I), from the hepatocyte/tumor cell compartment by AAV8-TBG-Cre led to inconclusive results, with increased liver body weight ratio and CK19^{+} tumor area in KRAS/p19 ICC, but slightly reduced liver-body

weight ratio and unaltered CK19^{+} area in YAP/AKT ICC (Figures 5J, 5K). In sum, our data show that neither COL1A1 nor DDR1 are essential for the ICC growth.

Myofibroblastic CAF promote tumor growth via hyaluronan synthase 2

We next investigated additional COL1A1-independent pathways through which myCAF, which strongly interacted with tumor cells (Figure 6A), could promote ICC growth. Focusing on differentially expressed matrisome genes in myCAF (Figure 6B), we identified hyaluronan synthase 2 (Has2) as one the most upregulated myCAF and panCAF genes (Figure 6B, Table S6). Of note, hyaluronan (HA) has been linked to tumor promotion, therapy resistance, and poor outcomes in various tumors including PDAC (McCarthy et al., 2018; Provenzano et al., 2012; Toole, 2004). CellPhoneDB analysis revealed multiple HA receptors including Cd44, Hmmr and Lyve1 on various cell types, reflecting the complex HA biology (Figures 6C, 6D). In addition to binding various receptors, HA bioactivity is also determined by receptor-independent biomechanical properties and its molecular size/degradation, with high-molecular weight HA being considered anti-tumorigenic and low-molecular weight HA being pro-inflammatory and tumor-promoting (Cyphert et al., 2015; Tian et al., 2013). For this reason, our primary focus was to investigate HAS2/HA as potential myCAF effector rather than defining its diverse cellular and receptor targets and mechanisms of action in ICC. Paralleling the high induction of Has2 mRNA in CAF, HA was abundant in both ICC models (Figure 6E), co-localizing with CAF but not with tumor cells (Figures S6A, S6B) and decreasing strongly after depleting HSC-CAF (Figures S6C–D). The predominant expression of HA in myCAF was shown by higher HA in Col1a1-GFP^{high} than in Col1a1-GFP^{low} TdTom^{+} HSC-CAF in murine ICC (Figure S6E). To determine the role of HAS2, we crossed Has2$^{fl/fl}$ mice with Lrat-Cre mice (Has2$^{\Delta HSC}$), resulting in >98.5% reduction of *Has2* mRNA in HSC and reduced HA in ICC (Figure S6F). Tumors were significantly decreased *Has2*$^{\Delta HSC}$ mice in both ICC models, with decreased liver body ratio and CK19^{+} tumor area (Figures 6F, 6G). Different from *Col1a1*$^{\Delta HSC}$ mice, tumors from *Has2*$^{\Delta HSC}$, did not show differences in stiffness (Figure 6H) or YAP/TAZ expression (Figure 6I). Consistent with our findings in CAF-depleted mice, *Has2*$^{\Delta HSC}$ tumors showed a significant reduction of tumor cell proliferation (Figure 6J). The deletion of *Cd44*, widely considered the main receptor for HA, from the hepatocyte/tumor cell compartment was efficient but did not reduce ICC development (Figures 6K, S6G, S6H). Moreover, different molecular weight and types of HA failed to induce tumor cell proliferation in CCA cell lines (Figure S6I). Likewise, the modest increase of proliferation by conditioned media from *Has2*-transgenic HSC (Yang et al., 2019) was not blocked by hyaluronidase treatment or CD44 antibody (Figures S6J, S6K). Together with our CellPhoneDB analysis, these findings suggest that HAS2 mediates its tumor-promoting effects through interactions with non-tumor cells or receptors other than CD44. HA was also significantly increased in human ICC and co-localized with CAF but not with tumor cells (Figures 6L, S6B, S6L, S6M). Importantly, tissue microarray analysis revealed a strong trend towards worsened survival in CCA patients with higher HA expression (Figures 6M; Figure S6L). Similar to our findings in mice, *HAS2* was expressed in HSC-CAF, and within those in the myCAF subpopulation in human ICC and CCA (Figures 6N; Figure S6M). Similar to mice, CellPhoneDB showed significant interactions between myCAF and tumor cells in human ICC, but also revealed interactions of *HAS2*-expressing CAF with multiple

HA receptors, including *CD44*, *HMMR*, and *LYVE1*, and multiple cell types (Figures 4D, S6N, S6O).

Inflammatory CAF promote ICC via HGF-MET

iCAF represented 48.5±2.3% of CAF in murine ICC, 53.1±6.2% of CAF in human ICC (Figure 4A) and 14% in human CCA. iCAF interacted strongly with tumor cells in CellphoneDB (Figures 4D, 7A). To identify candidate through which iCAF may modulate ICC growth, we analyzed scRNA-seq data for ligand-receptor interactions focusing on differentially expressed cytokines and growth factors (Figure 7B). Among these, we uncovered HGF-MET as well-established growth promoting ligand-receptor pair, with high relevance for liver regeneration (Michalopoulos and DeFrances, 1997) and the TME (Hanahan and Coussens, 2012). Notably, HGF is abundantly expressed in HSC and CAF (Friedman, 2008; Kalluri, 2016). Complementary to the strong expression of *Hgf* in iCAF, its receptor *Met* was highly expressed in tumor cells (Figures 7C, 7D), thus representing a candidate ligand-receptor pair direct linking CAF to tumor cells. The higher expression of HGF in iCAF than in myCAF was validated by ELISA (Figure S7A). Using RNAScope and IHC, we confirmed that *Hgf* and *Has2* mRNA as well as HA and RGS5 were localized in distinct HSC-CAF subsets in mouse and human ICC, respectively (Figures S7B, S7C). Next, we deleted *Hgf* in HSC-derived CAF via *Lrat*-Cre ($Hgf^{\Delta HSC}$), which was highly efficient (Figure S7D). $Hgf^{\Delta HSC}$ mice displayed reduced ICC development, with decreased liver body ratio and $CK19^{+}$ tumor area in our two ICC models (Figures 7E, S7E). Conversely, the deletion of HGF receptor *Met* in the hepatocyte/tumor compartment significantly reduced ICC growth (Figure 7F). HGF promoted proliferation in human and murine CCA tumor cells, including the newly established KRAS/p19-derived CGKP19 line (Figures 7G, S7F, S7G), confirming direct effects of HGF on tumor cells. Moreover, Ki67-positive tumor cells were significantly reduced in the $Hgf^{\Delta HSC}$ and $Met^{\Delta Hep}$ ICC models (Figures 7H, S7H). Phospho-kinase screening and immunoblotting revealed strong phosphorylation of ERK and AKT in HGF-treated human and mouse tumor cells, and HGF-induced proliferation was blunted after pharmacologic ERK inhibition (Figures 7I, 7J, S7I–K). As *in vivo* correlate, we observed a strong reduction of phospho-ERK in ICC in $Hgf^{\Delta HSC}$ mice (Figure 7K). scRNA-seq validated the high expression of *HGF* in HSC-derived iCAF in human ICC and CCA, while *MET* was expressed in tumor cells (Figure 7L, S7L). CellPhoneDB in ICC and CCA patients confirmed strong interactions between iCAF and tumor cells (Figure 4D) including interactions *via* iCAF-expressed *HGF* and tumor-expressed *MET* (Figures 7M, S7M). Together, these findings suggest the HGF-MET axis as key tumor-promoting ligand-receptor pair, directly linking iCAF to tumor cells in mice and patients via ERK-mediated tumor cell proliferation.

DISCUSSION

Our study, combining depletion, inhibition, and conditional knockout strategies in mice with survival analysis in two patient cohorts, firmly establishes a tumor-promoting role of CAF in ICC, contrasting their largely tumor-repressive role in PDAC (Ozdemir et al., 2014; Rhim et al., 2014). Moreover, our scRNA-seq, CellPhoneDB and co-injection studies suggest that tumor-promoting effects of CAF are mediated through direct HSC-CAF-tumor interactions,

but do not exclude the presence of additional tumor-promoting mechanisms, including immunomodulation. We found (i) similar CAF ontogeny with SC- and mesothelial/PF-derived CAF as the main populations in PDAC; (ii) employed KRAS as tumor driver and the same CAF depletion strategy as previous studies in PDAC (Ozdemir et al., 2014). However, while SC-CAF are abundant in early-stage PDAC, mesothelial CAF appear to be more abundant in advanced PDAC (Hosein et al., 2019). Thus, differences in CAF subtype or differences in tumor biology are more likely contribute to different roles of CAF in ICC and PDAC rather than different technical or depletion approaches. Even though PF/mesCAF were rare in ICC, we cannot exclude that they contribute to ICC growth.

Recent studies in various cancers have revealed CAF diversity (Biffi and Tuveson, 2020; Chen and Song, 2019; Costa et al., 2018; Elyada et al., 2019; Ohlund et al., 2017; Su et al., 2018; Zhang et al., 2020a) but the functions of specific CAF subtype mediators remain poorly understood. Here, we assign specific *in vivo* functions to iCAF and myCAF mediators *via* CAF-selective knockout to prove causation, thus complementing previous *in vitro* studies on CAF subtypes in breast cancer (Costa et al., 2018; Friedman et al., 2020) and PDAC (Elyada et al., 2019; Ohlund et al., 2017). iCAF represent growth factor- and cytokine-enriched HSC-CAF in a lower activation status expressing high levels of *HGF*, while myCAF are strongly activated HSC-CAF, enriched in *COL1A1* and *HAS2*/HA. Our *in vivo* data suggest that HGF and HAS2 represent distinct iCAF and mCAF mediators and that their pro-tumorigenic effects converge at the level of tumor cell proliferation. With fibrosis-associated HSC and HSC-CAF sharing most genes and pathways and iCAF and myCAF subpopulations displaying different degrees of fibroblastic activation, we propose that HSC first differentiate into iCAF, which subsequently give rise to myCAF. It is likely that the iCAF and myCAF states are transient and that CAF can shuttle between these states. CellPhoneDB analysis, *in vitro* studies as well as conditional knockout studies, suggested different mechanisms through which iCAF and myCAF mediators affect tumor cells, with iCAF-associated HGF acting directly on tumor cells and myCAF-associated HA possibly acting indirectly. Hence, these CAF subtype mediators represent potential therapeutic targets. While clinical targeting of HA has proven to be difficult, possibly because of inflammation mediated by degradation products (Cyphert et al., 2015; Ramanathan et al., 2019), targeting the HGF-MET pathway is clinically established with several FDA-approved drugs (Comoglio et al., 2018). Further studies are needed to identify the target cell(s) and the underlying receptor-dependent or receptor-independent mechanisms through which myCAF-expressed *HAS2*/HA operate. However, the finding that depletion of myCAF *via* αSMA-driven thymidine kinase reduces tumor growth in ICC while increasing tumor aggressivness and mortality (despite decreased tumor size) in PDAC may point toward a stronger rationale for targeting HA in ICC than in PDAC.

Surprisingly, abolishing CAF-derived type I collagen in this highly desmoplastic tumor did not reduce growth despite reduced stiffness, thus challenging a long-standing paradigm that links collagen-mediated stiffness to desmoplastic tumor growth (Barbazan and Matic Vignjevic, 2019; Levental et al., 2009; Northey et al., 2017). Our *in vitro* data, showing increased tumor cell proliferation on stiff plates, in conjunction with our *in vivo* data, revealing decreased stiffness and decreased YAP expression in tumors from *Col1a1*-deleted mice, suggest that type I collagen may activate tumor-promoting mechanosensitive and

additional tumor-suppressive pathways in parallel; and that the balance of these two determines the net effect, which was unaltered tumor growth in *Col1a1*$^{\Delta HSC}$ ICC. It is possible that type I collagen-mediated tumor suppression in ICC is due to its function as mechanical barrier (Egeblad et al., 2010; Liotta, 1986) and that the tumor-restrictive functions of αSMA^{+} myCAF in PDAC, observed in depletion experiments (Ozdemir et al., 2014; Rhim et al., 2014) are due to their ability to establish a mechanical barrier *via* type I collagen.

Future studies need to determine if iCAF and myCAF populations promote tumor growth through similar pathways in other desmoplastic tumors including extrahepatic cholangiocarcinoma; and whether myCAF- and iCAF-secreted HGF and HA represent therapeutic targets for ICC. As our analyses focused on European and North American cohorts and as racial background may affect CAF signature enrichment (Table 1), it would also be important to extend our studies to ICC from other regions such as Asia, where the underlying pathophysiology and genetic drivers differ due to high prevalence of fluke infections. While clinical studies targeting CAF in PDAC have been disappointing (Catenacci et al., 2015; Ramanathan et al., 2019), the potent tumor-promoting role of CAF and CAF mediators in ICC, contrasting tumor-suppressive effects of αSMA^{+}CAF in PDAC, may provide a stronger rationale for targeting CAF or their mediators in ICC.

STAR METHODS

RESOURCE AVAILABILITY

Lead Contact—Further information and requests for resources and reagents used in this study should be directed to the Lead Contact and corresponding author, Robert F. Schwabe (rfs2102@cumc.columbia.edu).

Materials Availability—The materials used in this study are listed in the Key resources table. Materials generated in our laboratory are available upon request.

Data and Code Availability—The RNA-seq and sc-RNA-seq data reported in this study have been deposited in the Gene Expression Omnibus database (GEO) under the accession number GSE154170. A previously published cohort of clinically annotated intrahepatic cholangiocarcinoma (Sia et al., 2013) of 119 patients (GSE32225) was used to determine the association between panCAF and myCAF gene expression signatures and survival and other clinical parameters. The human ICC sc-RNA-seq data analysis were based on the Zhang, M. et al; J Hep, 2020 GEO: GSE142784 and the Ma et al.; Cancer Cell, 2019 GEO:GSE125449. To identify the ontogeny of CAF in PDAC, we analyzed scRNA-seq data from KPC-induced mouse PDAC, using the Hosein et al.;2019 GEO:GSE125588.

EXPERIMENTAL MODEL AND SUBJECT DETAILS

Human Specimens—Fresh surgical tissue for single cell RNA-sequencing was obtained from a hilar, mainly extrahepatic cholangiocarcinoma with invasion of liver, gallbladder and periductal tissue cholangiocarcinoma patient (n=1) undergoing surgical resection at Columbia University Irving Medical Center. Written informed consent was obtained from

the patient at study entry and the study was approved by Columbia University Medical Center Institutional Review Board (IRB) (protocol number: IRB-AAAN7562). Frozen tissues and paraffin slides from paired tumor and non-tumor intrahepatic cholangiocarcinoma cases were used to extract RNA and perform IHC, respectively. Written informed consent was obtained from each patient at the time of recruitment and samples were collected under the supervision of the Columbia University Medical Center Institutional Review Board (Protocol Number: IRB-AAAN2452-M01Y06). Patient records were anonymized and de-identified. Studies were conducted in accordance with National Institutes of Health and institutional guidelines for human subject research. Two tissue microarrays (TMA) were constructed from formalin-fixed and paraffin-embedded tumor tissues of 19 intrahepatic cholangiocarcinoma (ICC), 59 extrahepatic cholangiocarcinoma (ECC), 39 gallbladder carcinoma (GBC) and 20 normal liver tissues at Department of Pathology and Molecular Pathology, University Hospital Zurich as previously described (Kononen et al., 1998; Riener et al., 2010). GBC samples were not analyzed in the current study. Clinicopathological features have been previously described (Riener et al., 2010) and the study was approved by the local ethics committee (PB_2018_00252).

Mice—All animal care and experimental procedures were performed in accordance with the "Guide for the Care and Use of Laboratory Animals" of the National Institutes of Health and were approved by Columbia University Institutional Animal Care and Use Committee. C57BL/6J, *TdTomato* Ai14 reporter (lox-stop-lox) (TdTom), *Rosa26*-iDTR (lox-stop-lox-*Hbegf* Cre-inducible diphtheria toxin receptor) transgenic mice (iDTR), *Rag2* KO and *Mx1*-Cre mice were obtained from the Jackson Laboratory. *Ddr1*^{tm1a} mice were obtained from Infrafrontier. *Col1a1*-GFP reporter mice (Krempen et al., 1999) and *Lrat*-Cre mice (Mederacke et al., 2013) were previously described and at least five time backcrossed to C57Bl/6. For HSC-selective deletion of *Col1a1*, *Hgf, Has2* and *RelA*, *Lrat*-Cre mice were crossed with mice carrying floxed alleles of *Col1a1* (Buchtler et al., 2018), *Hgf* (Phaneuf et al., 2004), *Has2* (Matsumoto et al., 2009) and *RelA* (Algul et al., 2007). For genetic HSC depletion, Lrat-Cre^{+} iDTR^{+} TdTom or LratCre^{+} iDTR^{-} TdTom controls were injected with diphtheria toxin (Sigma, i.p. 0.5 μg/kg) as indicated. For depletion of -αSMA^{+} CAF, mice expressing αSMA-driven thymidine kinase (αSMA-TK) (Ozdemir et al., 2014), kindly provided by Raghu Kalluri and at least five time backcrossed to C57Bl/6, were injected with ganciclovir (InvivoGen,10 mg/kg) as indicated. For HAS2 overexpression in -αSMA^{+} HSC, αSMA-*HAS2*Tg mice (Yang et al., 2019) were used. *Mx1*-Cre activation for the deletion of *Col1a1* was induced by 3 i.p. injections of poly(I:C) (10mg/kg; GE Healthcare), given every other day before or after tumor induction, as specified in the figure legend. To generate mice with *Ddr1* conditional potential, *Ddr1*^{tm1a} mice were bred with mice expressing *Ella*-driven flippase. For deletion of *Ddr1*, *Met* (Huh et al., 2004), and *Cd44* (kindly provided by Puré E.), four week old mice were infected with an AAV8-TBG-Cre (1×10^{11} genome copies i.v.) as described (Mu et al., 2016). Male mice, aged 6–8 weeks old (unless otherwise specified) were used for the experiments. All mice were housed in a specific pathogen-free facility, in microisolators in ventilated racks, and fed a regular chow diet. Animal care and experimental procedures were approved by Columbia University Institutional Animal Care and Use Committee.

Cell Lines—Human intrahepatic cholangiocarcinoma cell line HuCCT-1, cholangiocarcinoma cell line MzChA-1, and mouse SB1 intrahepatic cholangiocarcinoma cell line (Rizvi et al., 2018a) were a kind gift from Dr. Gregory Gores. Cells, including the CGKP19 cell line that we generated and described in method details, were cultured in DMEM with 10% FBS and antibiotics.

METHOD DETAILS

Liver Fibrosis Mouse Models—Biliary liver fibrosis was induced in eight-weeks-old mice subjected to ligation of the common bile duct (BDL) as previously described (Pradere et al., 2013). Mice were euthanized 14 days after the surgery. As a second model of well-established cholestatic liver fibrosis, mice were treated with diet containing 0.1% 3,5-diethoxycarbonyl-1,4-dihydrocollidine (DDC) for three weeks (Caviglia et al., 2018).

Plasmids and Cholangiocarcinoma Mouse Models—Sleeping beauty transposase SB13, pCaggs-*KRAS*^{G12D} (human) transposon plasmid and CRISPR/Cas9 sg-p19 (pX330-sg-p19) were provided by L. Zender, University of Tübingen, Germany. pT3-EF1α-HA-myr-Akt (mouse), pT3-EF1α-YAPS127A (human), pT3-EF1a-HA-FBXW7ΔF (human), pT3-EF1α-NICD1 (mouse) were previously described (Fan et al., 2012; Wang et al., 2018; Wang et al., 2019). A tumor-selective GFP reporter plasmid was constructed using the CK19 promoter to drive GFP expression (pT3-CK19-GFP). The NICD1/AKT, YAP/AKT and FBXW7ΔF/AKT ICC models have been previously described (Wang et al., 2018; Wang et al., 2019). For induction of ICC, plasmids were injected into six to seven weeks old mice by hydrodynamic tail vein injection (HDTV) at 20 μg:5 μg ratio of transposon to transposase-encoding plasmid (YAP/AKT, NICD/AKT and FBXW7ΔF/AKT models) or 25 μg:5 μg ratio of transposon to transposase-encoding plasmid and 10μg CRISPR/Cas9 sgRNA-p19 plasmid (KRAS/p19 model).

Generation of a Cholangiocarcinoma Cell Line—Mice were injected by HDTV with *KRAS*^{G12D} and CRISPR/Cas9 sg-p19 together with 40 μg of pT3-CK19-GFP plasmid. For tumor cell isolation, mouse livers were perfused six weeks later through the inferior vena cava as described (Mederacke et al., 2015), using increased concentrations of collagenase. Tumors were separated, mechanically dissociated and further digested with trypsin-EDTA (Gibco) and DNase (Roche) and sorted for GFP by flow cytometry using a BD Aria II Cell Sorter. Cells were named CGKP19 and were grown in DMEM supplemented with antibiotics and 10%FBS. Their ability to give rise to CCA *in vivo* was confirmed by injecting 1×10^6 cells subcutaneously in the left flank or in the spleen of C57BL/6J mice. CK19 expression was confirmed by western blot and IHC.

Cell Culture—To determine cell proliferation, 5×10^4 cells were plated in 12 well plates in growth media for 24 hours and after overnight starvation, were treated with recombinant human or recombinant mouse HGF 25 ng/ml (R&D) or vehicle in presence or absence of U-0126 ERK-inhibitor (Cayman Chemical) (5 μM) as specified in each figure legend. After 48 hours treatment, cells were fixed with 4% PFA and stained with HOECHST (ThermoFischer Scientific) 1:10000 in PBS, visualized with Olympus IX71S1F-3 microscope and counted using Fiji Software. Proteome Profiler Human Phospho-Kinase

Array Kit (R&D) was used to determine the phosphorylation of multiple kinases in human HuCCT-1 and in mouse CGKP19 cell lines after 10 minutes incubation with HGF at 25 ng/ml, accordingly to manufacturer's instructions. Quant-iT PicoGreen dsDNA Assay Kit (ThermoFisher Scientific) was used to measure proliferation assessed as the amount of double-stranded DNA (dsDNA) accordingly to the manufacturer's instructions, in HuCCT-1 plated on 2kPa, 16 kPa and 64 kPa plates (SoftSubstrates, MuWells) for 72 hours. BrdU cell proliferation assay was assessed as previously described with some modifications (Yang et al., 2019). Briefly, primary HSCs isolated from wild type or αSMA-*HAS2*Tg mice were cultured for 7 days and then supernatants were collected. Tumor cells, starved overnight in 0.1% FBS medium, were treated with the HSC conditioned medium (HSC-CM) for 20 to 36 hours. The BrdU was added to culture medium and incubated for additional 5 to 24 hours. BrdU incorporation was assessed according to manufacturer's instruction (Millipore Sigma). For the hyaluronidase treatment, supernatants from HSC culture were incubated with hyaluronidase (Sigma) with a final concentration 100 U/mL for 1hr at 37°C. Hyaluronic acid concentration was measured by using Hyaluronan ELISA Duo set according to manufacturer's instruction (R&D systems). For CD44 blocking experiments, tumor cells were treated with anti-mouse CD44 antibody (Cedarlane, clone:KM-81) with a final concentration 0.2 •g/mL for 1 hour, and then treated with HSC-CM. Rat IgG2a (ThermoFischer Scientific) was used as control. For HA treatment, tumor cells were cultured with DMEM supplemented with 10%FBS and antibiotics for 24 hours. After starvation, cells were treated with hyaluronan low molecular weight (R&D), hyaluronan medium molecular weight (R&D), hyaluronan high molecular weight (R&D), HA Potasium salt from cockscomb (Carbosynth), HEALON® PRO OVD (Johnson and Johnson Vision) and hyaluronic acid sodium salt from rooster comb 100 μg/mL (Millipore Sigma) all at 100 μg/mL. After 36hours, the BrdU was added to culture medium and the cells were incubated for additional 3 hours. BrdU incorporation was assessed according to manufacturer's instruction (Millipore Sigma).

HSC and CAF Isolation—Mouse HSC were isolated by *in situ* liver perfusion as described (Mederacke et al., 2015; Pradere et al., 2013), the cells were further purified by FACS using endogenous retinoid fluorescence (Mederacke et al., 2015) or by *Lrat*-Cre-induced TdTomato fluorescence. CAFs from *Lrat*-Cre^{+} TdTom *Col1a1*-GFP^{+} mice were isolated following above tumor cell isolation protocol with some modifications. Before FACS sorting, cells were subjected to a separation gradient using Nycodenz 34%. CAF were sorted for GFP; HSC-derived CAFs were sorted by GFP and TdTomato double positive signal, on a BD Aria II Cell Sorter, followed by RNA sequencing or scRNA sequencing.

Immune Cell Isolation and Flow Cytometry—Myeloid and lymphoid subsets were isolated from the tumors and quantitatively analyzed as previously described (Chowdhury et al., 2019) with some modifications. Briefly, after mechanical homogenization, the tumors were digested with collagenase A (1 mg ml−1; Roche) and DNase I (0.5 μg ml−1; Roche) in isolation buffer (RPMI 1640 supplemented with 5% FBS, 1% L-glutamine, 1% penicillin–streptomycin and 10 mM HEPES) for 45 minutes shaking (150 rpm) at 37 °C. Cells were filtered through 100 μm cell strainers, washed in isolation buffer and stained. Myeloid cells were stained immediately, and lymphoid subset underwent a separation gradient using

Percoll (67%, 40%), followed by staining. Dead cells were excluded by staining with Ghost Dye cell viability reagent. Extracellular antibodies included: anti-B220 (BD) (1:200), anti-CD19 (Tonbo) (1:200), anti-CD45 (BD and Biolegend) (1:400), anti-CD4 (BD) (1:400), anti-CD8 (Tonbo) (1:400), anti-NK1.1 (BD) (1:300), anti-CD11b (BD) (1:500), anti-CD11c (BD) (1:200), anti-F4/80 (Tonbo) (1:500), and anti-MHC class II (Tonbo) (1:400) antibodies. Intracellular antibodies included: anti-CD3e (BD) (1:400), anti-TCRβ (BD) (1:300) and anti-FOXP3 (Thermo) (1:300). Cells were fixed using the FOXP3/transcription factor staining buffer set (Tonbo) according to the manufacturer's protocol. Samples were analyzed using a BD LSRFortessa cell analyzer.

Rheometry—Tumor samples were cut from livers using a stainless-steel punch when >8mm, and cylindrical samples were cut manually when <8mm and the diameter was determined from optical images. Parallel plate shear rheometry was carried out using a Kinexus rheometer (Malvern Panalytical, Westborough, MA). Samples were attached to the top and bottom plates with fibrin glue made by mixing 10 μl of 5 mg/ml salmon fibrinogen and 10 μl of 150 U/ml salmon thrombin (Sea Run Holdings, Freeport, ME) for each side of the sample. The upper plate (8 mm diameter) was lowered until contact was made as determined by the application of 400 Pa normal stress, and the sample was allowed to sit for 5 min to ensure attachment to the metal plates. Shear storage modulus G', loss modulus G", and normal force were measured by applying a low oscillatory shear strain of 2% at a frequency of 1 rad/sec at room temperature. Simultaneously, samples were subjected to small stepwise axial strains in tension (0, 10, and 20%) followed by compression (−10, −15, −20, and −25%), between which the samples were allowed to relax for 2 min. Samples were kept hydrated during experiments with PBS. The equilibrium G' and G" after 2 min of relaxation were plotted against axial strain.

Immunoblotting—Whole-cell and tissue extracts were prepared using RIPA buffer containing PhosSTOP phosphatase inhibitor (Roche) and cOmplete protease inhibitor (Roche). Proteins were subjected to 10% SDS–PAGE and blotted on a nitrocellulose membrane (Sigma) with a semi-dry blot system (BioRad). Membranes were incubated with the following primary antibodies: p-ERK1/2 (1:2000, Cell Signaling, #4370), ERK1/2 (1:1000, Cell Signaling, #4695), p-AKT (1:2000, Cell Signaling, #4060), AKT (1:1000 Cell Signaling, #9272), YAP/TAZ (1:1000, Cell Signaling, #8418), DDR1 (1:1000, Cell Signaling, #5583) followed by incubation with horseradish peroxidase-conjugated secondary antibody against rabbit IgG (1:5000, Santa Cruz, #sc-2004). GAPDH (1:15000, Sigma, #G9295) was used as loading control. Blots were visualized using SuperSignal™ West Femto Maximum Sensitivity Substrate (ThermoFisher Scientific) and bands were quantified with ImageJ software. If necessary, stripping was performed with Restore Western Blot Stripping Buffer (ThermoFisher Scientific).

Enzyme-linked Immunosorbant Assay—CAFs from *Lrat*-Cre^{+} LSL-TdTom *Col1a1*-GFP^{+} mice were isolated following the above CAF isolation protocol from YAP/AKT and KRAS/p19-induced ICC models. iCAF were sorted by GFP^{low} and TdTomato double positive signal, and myCAF were sorted by GFP^{high} and TdTomato double positive signal on a BD Aria II Cell Sorter and were quickly plated in a high binding 96-well plate (Greiner

Bio-one) in white DMEM supplemented with 10% FBS and antibiotics. 24 hours later the supernatants were collected and used to perform the Mouse HGF DuoSet ELISA (R&D) following the manual's instructions. To increase the sensitivity, we used the QuantaBlu™ Fluorogenic Peroxidase Substrate Kit (ThermoFisher Scientific) to detect the signal. The SpectraMax iD3 (Molecular Devices) microplate reader was used to detect the signal and read the results.

Immunohistochemistry and Immunofluorescence—Paraffin-embedded or frozen liver sections 5-μm thickness, were incubated with the following primary antibodies: CK19 (1:500, Abcam), CK7 (1:2000, ThermoFisher), Ki67 (1:100, Abcam and 1:100 e-Biosciences), cleaved caspase-3 (1:200, Cell Signaling), CD3 (1:200, Abcam), p-ERK1/2 (1:300, Cell Signaling), α-SMA (1:250, Sigma), SERPINF1 (1:200, NovusBio), RGS5 (1:50 Abcam). For detection of hyaluronic acid in liver sections and TMAs, HABP recombinant protein (rhAggrecan aa20–675/His [NSO/7], biotinylated, R&D Systems) was used at a concentration of 4 μg/ml, as previously described (Yang et al., 2019). Detection was performed using either the Vectastatin Elite ABC-HRP kit (Vector Laboratories) with DAB Peroxidase Substrate kit (Vector Laboratories) or a fluorescent secondary antibody with various fluorescent conjugates (donkey anti-rabbit Alexa Fluor 488, 1:500, Life Technologies; donkey anti-mouse Alexa Fluor 488, 1:500, Life Technologies) with streptavidin signal amplification (Alexa Fluor 594/647, 1:500, Life Technologies), followed by counterstaining with either hematoxylin or DAPI (Thermo Fisher Scientific). IHC for smooth muscle actin (1:350, Nordic Biosite) in the TMAs, was performed using the conventional Ventana BenchMark platform (Roche®) and OptiView DAB kit for secondary antibody and color development (760–700, Roche®). Non-fluorescence image acquisition was performed with a Leica SCN400 slide scanner or Olympus IX71S1F-3 microscope coupled to a QImaging Retiga camera. Quantification of DAB positive area was performed using the LEICA Digital Image Hub 4.0 image server. Fluorescence images were captured at 10x, 20x or 40x magnification using Olympus IX71S1F-3 microscope or Nikon A1 confocal laser microscope (Nikon Instruments). Images were analyzed using Fiji ImageJ and Adobe Photoshop. *Col1a1*-GFP and RGS5, HA and RGS5, SERPINF1 and RGS5 costainings were quantified by measuring the stained area for each antibody in a specific cell; counting was evaluated in n=20 ±5 cells for each tumor (n=3) and the cells were categorized into high and low using the median as cut-off and the ratio was determined.

RNAscope—Frozen liver sections 10-μm thickness from two different cholangiocarcinoma mouse models (YAP/AKT and KRAS/p19) were obtained from *Lrat*-Cre LSL-*TdTomato* mice and were imaged with RNAscope. The RNAscope® Multiplex Fluorescent Reagent Kit v2 including RNAscope Multiplex Fluorescent Detection Kit (PN 323110), RNAscope H202 and Protease Reagents (PN 322381) and RNAscope Target Retrieval reagents (322000), RNAscope Wash Buffer (PN 310091), the pretreatment TSA buffer (322809), and detection reagents for manual amplification from Advanced Cell Diagnostic were used to spatially detect *via* in situ hybridization *Hgf* and *Has2* using the RNAscope® Probe-Mm-*Hgf*-C3 (ACD;Cat No. 315631-C3) and the RNAscope® Probe-Mm-*Has2*-C2 (ACD;Cat No. 465171-C2) specific probes respectively, following the RNAscope Multiplex Fluorescent v2 Assay Protocol, optimized for fixed-frozen samples. Chromogenic detection

was performed using a horseradish peroxidase (HPR) construct specific to each gene-dedicated imaging channel and a fluorescent Opal reagent. *Has2* was stained with Opal 520 Reagent (Perkin Elmer, FP1487001KT), and *Hgf* was stained with Opal 690 Reagent (Perkin Elmer, FP1488001KT). Each Opal reagent dye was diluted 1:1500 in RNAscope® Multiplex TSA Buffer. Nuclei were stained with DAPI (4′,6-diamidino-2-phenylindole) and coverslips were mounted over slides in Fluoro-Gel (EMS; 17985–10) and imaged by a Nikon A1 confocal laser microscope (Nikon Instruments). Images were analyzed using Fiji ImageJ. For each model (YAP/AKT and KRAS/p19) 5 tumors were evaluated. The *Hgf* and *Has2* stained area in a specific cell was evaluated in n=20 ±8 cells for each tumor and the cells were categorized into high and low gene expression using the median ratio as cut-off.

Fibrosis Quantification—Hepatic fibrosis was determined by picrosirius red staining as previously described (Pradere et al., 2013). Pictures for quantification of picrosirius red staining were taken in a minimum 5 low-power fields/mouse using a polarized light filter and quantified by Adobe Photoshop software.

RNA Isolation and qPCR—Total RNA was isolated from cells and liver tissue by column purification and on column DNAse treatment (Roche Diagnostics). Following reverse transcription using High Capacity cDNA Reverse Transcription Kits (Applied Biosystems), mRNA levels were determined by quantitative real-time PCR on Applied Biosystems™ QuantStudio™ 5 Real-Time PCR System, using PerfeCTa qPCR FastMix (Quanta) and ABI Taqman primer-probes. All qPCRs were quantified using relative standard curves and normalized to expression of 18s.

Bulk RNA Sequencing—RNA was extracted using the RNeasy Micro or Mini Kit (Qiagen) with on-column DNAse digestion accordingly to manufacturer instructions. RNA (RNA integrity number [RIN] >8, as determined by Bioanalyzer 2100, Agilent Technologies) was used to construct libraries using Illumina TruSeq RNA Preparation Kit according to the manufacturer's instructions. 20M paired-end 100bp sequencing was performed using the Illumina NovaSeq 6000 at Columbia Genome Center. RTA (Illumina) was used for base calling and bcl2fastq2 (version 2.19) for converting BCL to fastq format, coupled with adaptor trimming. A pseudoalignment to a kallisto index was created from transcriptomes (Human: GRCh38; Mouse: GRCm38) using kallisto (0.44.0). Differentially expressed genes were tested using DESeq2. Normalization was done internally using DESeq2's specialized algorithm and normalization to compare across samples, was performed using the TPM (transcripts per million) method. All heatmaps were generated using the ComplexHeatmap R/bioconductor package v2.4.2 (Gu, Z. (2016). Complex heatmaps reveal patterns and correlations in multidimensional genomic data. The functional enrichment analysis was performed using g:Profiler (version e99_eg46_p14_f929183) with g_SCS multiple testing correction method applying significance threshold of 0.05 (Raudvere et al., 2019; Reimand et al., 2019).

Single Cell RNA-Sequencing—CAF-enriched but diverse cell populations from KRAS/p19- and YAP/AKT-induced ICC tumor specimens were obtained following isolation protocol described above for CAF from *Lrat*-Cre^{+} LSL-*TdTomato Col1a1*-GFP^{+} mice. For

n=2 YAP/AKT ICC samples (YAP/AKT ICC1 and YAP/AKT ICC3), cells were sorted for *Col1a1*-driven GFP. To obtain CAF-enriched samples containing multiple cell populations for a more detailed CellPhoneDB analysis, we combined *Col1a1*-GFP$^+$ cells (70%) from n=1 YAP/AKT (YAP/AKT ICC2) and n=1 KRAS/p19 ICC sample with the respective unpurified cell suspension (30%) after sorting on a BD Aria II Cell Sorter. Tumor specimen from above described CCA patient was freshly dissociated, minced to 2–4 mm sized pieces and subsequently digested to single cell suspension using Multi Tissue Human Tumor Dissociation Kit 1 (Miltenyi Biotec) and a gentleMACS OctoDissociator (Miltenyi Biotec) according to the manufacturer's instructions. The dissociated sample was processed for scRNA sequencing and this sample is referred as "human CCA" in the manuscript. Previously published scRNA sequencing datasets of human ICC samples (Ma et al., 2019; Zhang et al., 2020b) were included. These datasets included as analysis are in total 6 human ICC samples, but one sample (GSE142784/GSM4240156_ICC32S = Human ICC4) contained an insufficient number of tumor cells for CellPhoneDB analysis. Specifically, sample ICC4 (GSM4240156_ICC32S - humanICC_S2D2) yielded 5661 cells in the raw counts data and 4892 cells after QC filtering with mitochondrial gene cut-off of 50% and UMI count threshold of 40,000, which was one magnitude higher than the 498 cells reported to be analyzed by Zhang et. Al, who used a very stringent mitochondrial gene cut-off. The slightly lower quality of this sample may have contributed to some minor discrepancies with other samples from our analysis. Samples and the associated downstream analyses are summarized in Table S1. Among these GSE142784/GSM4240155_ICC24S (Human ICC1) and GSE142784/GSM4240156_ICC32S (Human ICC4), were CAF-enriched samples, all others were non-enriched samples. From Zhang et al. (GSE138709 = Human ICC2), 5 tumors (GSM4116580, GSM4116581, GSM4116583, GSM4116584, GSM4116585) from 4 different patients were merged using "MergeSeurat" function in Seurat v2.4 (Stuart et al., 2019) and the raw counts were used for further analysis described in the methods. From these, only GSM4116585 (Human ICC2–1), GSM4116584 (Human ICC2–2) and GSM4116583 (Human ICC2–3) were included to investigate HSC-CAF/PF-CAF, iCAF/myCAF/mesCAF percentages and analyze ligand-receptor interactions by CellphoneDB as other samples did not have enough CAF for these analyses. From Ma et al (GSE125449 Set1 = Human ICC3), we extracted raw counts of 6 ICC patients: S11_P06_LCP29, S09_P04_LCP25, S08_P03_LCP26, S12_P07_LCP30, S20_P12_LCP35, S19_P11_LCP39. Only human S11_P06_LCP29 (Human ICC3–1) was included to investigate HSC-CAF/PF-CAF, iCAF/myCAF/mesCAF percentages and analyze ligand-receptor interactions by CellphoneDB as other samples did not have enough CAF for these analyses.

Single Cell RNA-Sequencing Analysis—Mouse and human tumor specimens were processed as previously described and freshly isolated cells were counted on Countess II automated cell counter (ThermoFisher) and were loaded on a 10x Chromium instrument (10x Genomics). Single-cell RNA-seq libraries were prepared using the Chromium Single Cell 3′ v2 or v3 Reagent Kit (10x Genomics) according to manufacturer's instructions. 12 cycles of cDNA amplification and 12 cycles of library amplification were performed, and samples were sequenced on an Illumina NovaSeq 6000 Sequencing System at the JP Sulzberger Columbia Genome Center. 10x Genomics Cellranger pipeline was used to process the data (YAP/AKT v2.1.1(ICC1), v4.0.0 (ICC2 and ICC3); KRAS/p19 and human

ICCs and hilar CCA v3.1.0). BCL files were demultiplexed with 10x Cell Ranger's mkfastq command and analysis and alignment were performed using Cell Ranger's count command with Cell Ranger's reference mm10. Single-cell count matrices were loaded into scanpy AnnData objects (scanpy v1.4.6) and ribosomal protein genes were removed. We analyzed QC metrics (total number of counts, number of genes detected, percentage of mitochondrial RNA) to identify and remove outliers in the distribution of cells (Ilicic et al., 2016). Each cell was normalized using pool-derived size factors (Lun et al., 2016) and each normalized matrix was then log-transformed. Principal component analysis was performed on the resulting matrices (scanpy v1.4.6). To identify significant principal components, we exploited Random Matrix Theory methodologies through the randomly algorithm (Aparicio L, 2020). We applied UMAP (McInnes, 2018) to visualize the distribution of cells in the projection of the significant principal components. UMAPs were used to show the normalized expression levels of indicated signatures and genes. To identify cell sub-populations, we chose the Louvain algorithm for community detection (Blondel VD, 2008) with different values for the resolution parameter, comparing the average Silhouette score across all cells for each clustering (Rousseeuw, 1987). Differentially expressed genes were computed using the Wilcoxon Rank-Sum test (as implemented in scanpy), and we labeled the different populations using the genes differentially up-regulated in each population. Cell populations including CAF, hepatocytes, T and B lymphocytes, dendritic cells, endothelial cells, myeloid cells, monocytes and neutrophils, were identified using specific markers genes (Table S2) and confirmed by PanglaoDB (Oscar Franzén, 2019). Mouse scores for panCAF and CAF subpopulation signatures were computed as previously defined (Elyada et al., 2019). Clusters having at least 49% of cells with positive pan-CAF score were considered further for analysis of CAF subtypes (mouse ICC panCAF signature: Col1a1, Col1a2, Col3a1, C1s1, Acta2, C1ra, Serpinf1, Pdgfrb, Col12a1). HSC-CAF and PF-CAF scores were calculated using the HSC and PF signatures in Table S2 and HSC-CAF, PF-CAF and other-CAF percentages of total pan-CAF were calculated for each sample. Some murine and human cells with the HSC-CAF cluster also expressed Myh11 and Actg2, vascular smooth muscle cell markers (Figure S1H), but they were positive for the HSC signature and were considered HSC (Table S2) since they did not cluster distinctly from HSC, suggesting that these cells represent an HSC-CAF subtype rather than an own entity. Another population sharing endothelial and HSC markers (emHSC) was found in mice from YAP/AKT-induced ICC, and was analyzed as a distinct cell population (Table S2); this population was negative for the panCAF score. Within panCAF, CAF subpopulation score distributions were analyzed, and a CAF subpopulation label was assigned to each cell if the corresponding score was higher than 0.125 (higher than 0 to reduce the number of cells with multiple labels). Afterwards, we sorted all cells into three sets: i) single-CAF (cells with a single label), ii) multi-CAF (cells with more than one label), iii) other-CAF (cells with no label). A new signature for different CAF subpopulations was computed on single-CAF for each sample by selecting differentially expressed genes between the different subpopulations ($q < 0.05$, log-FC > 1). Only single-CAF within each sample were considered in the previous step and 3 different populations were identified and named as iCAF, myCAF and mesCAF accordingly to their DGE and pathways enrichment (described in Results and Tables S4,S5). To produce a single-CAF consensus signature for each different CAF subpopulation, the genes differentially expressed for each population were refined by

keeping only i) genes present in both YAP/AKT ICC1 and KRAS/p19 samples signatures, and ii) genes that after step (i) were mutually exclusive between CAF subpopulations (iCAF, myCAF and mesCAF mouse signatures are displayed in Table S2). The inter-sample set of CAF subpopulations signatures (consensus signature) was then reapplied to panCAF of both samples, and the refined number of cells (and percentage) of the different labelled subpopulations was computed. In human ICC dataset, PDAC-defined CAF signatures (Elyada et al., 2019) and the mouse ICC CAF signatures were used to define the cell clusters corresponding to panCAF and CAF subpopulations iCAF, myCAF and mesCAF. The panCAF human signature was computed by obtaining the differentially expressed genes ($q < 0.05$, log-FC > 1) in panCAF cluster compared to all other cell types and manually selecting genes with panCAF specific expression (human panCAF signature: *COL1A1*, *COL1A2*, *COL3A1*, *C1S*, *ACTA2*, *C1R*, *SERPINF1*, *PDGFRB*). HSC-CAF and PF-CAF clusters were determined from the HSC and PF signatures in Table S2 as described previously in mouse. The CAF subpopulations iCAF, myCAF and mesCAF clusters obtained were independently validated by their differential gene expression and GO enrichment analysis. iCAF, myCAF and mesCAF signatures were computed by obtaining the differentially expressed genes ($q < 0.05$ and log-FC > 1 or top 20 genes) in the respective CAF subpopulation cluster compared to the rest of panCAF (human signature in Table S2). These panCAF and CAF subpopulation signatures were then reapplied to all human ICCs and CCA samples to obtain and quantify CAF populations as mentioned previously in mouse. The CAF subpopulation score threshold was selected to minimize the number of cells with multiple labels. The violins showing the signature scores were computed for each cells the difference between average expression of gene signature with average expression of a set of randomly selected genes. The width of each violin plot indicates the kernel density of the expression values.

Global Stellate Cell and PF Signatures—To identify the ontogeny of CAF in PDAC, we analyzed scRNA-seq data from KPC-induced mouse PDAC, using the ‘early KIC’ sample from GEO (GSE125588) (Hosein et al., 2019). To determine a gene signature that could identify both HSC PSC-derived CAF, we determined the top 100 differentially expressed genes between HSC-CAF and PF-CAF in KRAS/p19-induced ICC and YAP/AKT-induced ICC1, as well as between the fibroblast populations identified as “1“ and “2” (strongly marked by HSC marker *Cygb* and weakly marked by HSC markers *Des*, *Lrat* and *Rgs5*, hence candidate PSC-CAF) and as “3” in the original paper (Hosein et al., 2019) (marked by multiple mesothelial markers, hence candidate mesothelial CAF). Among these differentially expressed genes, 11 genes (see Table S2 and Figure S2) were identified as common to all three models and clearly differentiated HSC and PSC-derived CAF from PF-CAF in ICC or mesothelial CAF in PDAC. Thus, they form a global stellate cell signature. The global PF signature was based on the hepatic PF signature of *Msln*, *Gpm6a*, *Upk1b* and *Upk3b,* and included *Krt19,* in addition (Table S2).

CellPhoneDB Analysis—CellPhoneDB (Vento-Tormo et al., 2018), a curated repository of ligands, receptors, their subunit architectures and interactions with an integrated statistical framework to infer cell-cell communication networks between cell types in single-cell transcriptomics data, was used to identify ligand-receptor interactions in n=4 mouse samples of ICC, n=5 human ICC and n=1 human hilar CCA. After identifying different cell types in

our scRNA-seq datasets as described above, we followed recommended procedures for preparation of input files using CellPhoneDB v.2.0.0 (Vento-Tormo et al., 2018). We updated the original CellPhoneDB repository with novel interactions and complexes curated from literature using 'cellphonedb database generate' command. All CellPhoneDB statistical analysis were performed with this updated database and percentage cell expression threshold of 1%. Cell-cell interactions heatmaps showing number of interactions, Log2 mean (Molecule 1, Molecule 2) and log10(p value), were generated using pheatmap R package and ligand-receptor interactions were visualized using ggplot2 R.

Clinical Parameter Analysis in Human ICC—The association between panCAF and myCAF gene expression signatures and overall survival as well as other clinical parameters shown in Table 1, was tested in a previously published cohort of clinically annotated intrahepatic cholangiocarcinoma (Sia et al., 2013). Survival data were available for 119 patients along with matched whole-genome gene expression data (GSE32225). For the testing of human ICC *ACTA2*, panCAF signature: *COL1A1*, *COL1A2*, *COL3A1*, *C1S*, *ACTA2*, *C1R*, *SERPINF1*, *PDGFRB* and myCAF signature (see Table S2), an enrichment score was calculated for each patient using the single-sample Gene Set Enrichment Analysis (ssGSEA) methodology (Barbie et al., 2009) implemented in Gene Pattern (Reich et al., 2006). Patients were then categorized into high and low enrichment score or high and low gene expression using the median as cut-off. Kaplan-Meier method and log-rank test were performed to analyze the association of gene signatures and gene expression with overall survival using IBM SPSS version 24 (http://www.ibm.com/). Overall Survival was defined as the time between surgical resection and death of any cause or loss to follow-up. All reported p-values are 2-sided and $p<0.05$ was considered significant.

The association between HA expression and overall survival was tested in the above-described TMAs from the Riener (Riener et al., 2010) cohort by quantifying the percentage of the HA-positive stained area in ICC and ECC patients using Fiji ImageJ. Survival data were available for 16 ICC and 50 ECC patients. Patients were categorized into high and low HA expression using the third quartile as cut-off (cut-off=65.41). 16 patients (5 ICC and 11 ECC) had a score > 65.41 and 50 patients (11 ICC and 39 ECC) had expression < 65.41. The association between αSMA expression and overall survival was tested in the above-described TMAs by digitization using a Nano-Zoomer Digital Pathology scanner (Hamamatsu, Japan) at the maximum in-built magnification of 400X. Image analysis was processed in QuPath v.0.1.3 (Queen's University, Belfast, Northern Ireland). TMA slides were dearrayed and preprocessed as previously described (Bankhead et al., 2017). After dearraying, TMAs were manually curated. Cell-detection was conducted using QuPath's built-in "Positive cell detection" (Bankhead et al, 2017). For each core, the total number of positive cells, irrespective of localization, was assessed. Survival data were available for 17 ICC and 60 ECC patients. Patients were categorized into high and low αSMA expression using the median as cut-off (cut-off=34.71). 40 patients (11 ICC and 29 ECC) had a score > 34.71 and 37 patients (6 ICC and 31 ECC) had expression < 34.71. Kaplan-Meier method and log-rank test were performed to analyze the association of gene signatures and gene expression with overall survival using GraphPad Prism v.8.0.

QUANTIFICATION AND STATISTICAL ANALYSIS

GraphPad Prism v.8.0 was used for statistical analyses. D'Agostino-Pearson omnibus normality test, Anderson-Darling test and Shapiro-Wilk normality test were performed to assess data distribution. For statistical analysis of parametric data, the two-tailed unpaired Student's t test was used for groups of two; one-way ANOVA followed by Sidak multiple comparison posthoc tests for comparison of more than two groups. For non-parametric data, the Mann-Whitney U test was used for groups of two; Kruskal-Wallis test followed by Dunn multiple comparison posthoc test was used for comparison of more than two groups.

Supplementary Material

Refer to Web version on PubMed Central for supplementary material.

ACKNOWLEDGEMENTS

This work was supported by NIH R01CA228483 (R.F.S.,X.C.); R01CA190844 (R.F.S.); P30CA013696 (Columbia University Cancer Center); R01DK085252, P01CA233452 (E.S.); R01CA190606 (X.C.) and P30DK026743 (UCSF Liver Center); 5U54CA193417 (R.W.), US Department of Defense grant CA150272P3 (J.M.L.), R35CA197745; S10 OD012351, S10 OD021764 (A.C.); P01CA117969, Project 3 (R.K.); R03DK101863 (J.M.C); P01CA87497, R35CA209896, NINDS grant R61NS109407 (B.R.S). Swiss National Science Foundation SNF310030_146940 (A.W.,A.L.); Deutsche Forschungsgemeinschaft FOR2314, SFB-TR209, Gottfried Wilhelm Leibniz Program and ERC 'CholangioConcept' (L.Z.). S.A. was funded by an American Liver Foundation Postdoctoral Research Fellowship Award, a Cholangiocarcinoma Foundation's Innovation Award and a Research Scholar Award from the American Gastroenterological Association; S.B. by Deutsche Forschungemeinschaft grant GZ:BH 155/1–1; A.F. by Recherche Médicale's postdoctoral fellowship SPE20170336778, and an American Liver Foundation's Postdoctoral Research Award. We thank Drs. Liang Zhao and Ellen Pure (University of Pennsylvania) for CD44 floxed mice; Susanne Dettwiler, Fabiola Prutek, André Fitsche, Christine Mittmann and Marcel Glönkler (University of Zurich) for TMA sections and IHC; Dr. Gregory Gores (Mayo Clinic, Rochester, MN) for CCA cell lines; and Drs. Timothy Wang and Kenneth Olive (Columbia University) for critical reading.

REFERENCES

Affo S, Yu LX, and Schwabe RF (2017). The Role of Cancer-Associated Fibroblasts and Fibrosis in Liver Cancer. Annu Rev Pathol 12, 153–186. [PubMed: 27959632]

Algul H, Treiber M, Lesina M, Nakhai H, Saur D, Geisler F, Pfeifer A, Paxian S, and Schmid RM (2007). Pancreas-specific RelA/p65 truncation increases susceptibility of acini to inflammation-associated cell death following cerulein pancreatitis. J Clin Invest 117, 1490–1501. [PubMed: 17525802]

Aparicio L BM, Blumberg AJ, Rabadan R. (2020). A Random Matrix Theory Approach to Denoise Single-Cell Data. Patterns 5 4:100035. [PubMed: 33205104]

Banales JM, Marin JJG, Lamarca A, Rodrigues PM, Khan SA, Roberts LR, Cardinale V, Carpino G, Andersen JB, Braconi C, et al. (2020). Cholangiocarcinoma 2020: the next horizon in mechanisms and management. Nat Rev Gastroenterol Hepatol.

Bankhead P, Loughrey MB, Fernandez JA, Dombrowski Y, McArt DG, Dunne PD, McQuaid S, Gray RT, Murray LJ, Coleman HG, et al. (2017). QuPath: Open source software for digital pathology image analysis. Sci Rep 7, 16878. [PubMed: 29203879]

Barbazan J, and Matic Vignjevic D (2019). Cancer associated fibroblasts: is the force the path to the dark side? Curr Opin Cell Biol 56, 71–79. [PubMed: 30308331]

Barbie DA, Tamayo P, Boehm JS, Kim SY, Moody SE, Dunn IF, Schinzel AC, Sandy P, Meylan E, Scholl C, et al. (2009). Systematic RNA interference reveals that oncogenic KRAS-driven cancers require TBK1. Nature 462, 108–112. [PubMed: 19847166]

Biffi G, and Tuveson DA (2020). Diversity and Biology of Cancer-Associated Fibroblasts. Physiol Rev.

Blondel VD GJ-L, Lambiotte R, Lefebvre E. (2008). Fast unfolding of communities in large networks. J Stat Mech Theory Exp 10008:6.

Buchtler S, Grill A, Hofmarksrichter S, Stockert P, Schiechl-Brachner G, Rodriguez Gomez M, Neumayer S, Schmidbauer K, Talke Y, Klinkhammer BM, et al. (2018). Cellular Origin and Functional Relevance of Collagen I Production in the Kidney. J Am Soc Nephrol 29, 1859–1873. [PubMed: 29777019]

Catenacci DV, Junttila MR, Karrison T, Bahary N, Horiba MN, Nattam SR, Marsh R, Wallace J, Kozloff M, Rajdev L, et al. (2015). Randomized Phase Ib/II Study of Gemcitabine Plus Placebo or Vismodegib, a Hedgehog Pathway Inhibitor, in Patients With Metastatic Pancreatic Cancer. J Clin Oncol 33, 4284–4292. [PubMed: 26527777]

Caviglia JM, Yan J, Jang MK, Gwak GY, Affo S, Yu L, Olinga P, Friedman RA, Chen X, and Schwabe RF (2018). MicroRNA-21 and Dicer are dispensable for hepatic stellate cell activation and the development of liver fibrosis. Hepatology 67, 2414–2429. [PubMed: 29091291]

Chen X, and Song E (2019). Turning foes to friends: targeting cancer-associated fibroblasts. Nat Rev Drug Discov 18, 99–115. [PubMed: 30470818]

Chowdhury S, Castro S, Coker C, Hinchliffe TE, Arpaia N, and Danino T (2019). Programmable bacteria induce durable tumor regression and systemic antitumor immunity. Nat Med 25, 1057–1063. [PubMed: 31270504]

Clements O, Eliahoo J, Kim JU, Taylor-Robinson SD, and Khan SA (2020). Risk factors for intrahepatic and extrahepatic cholangiocarcinoma: A systematic review and meta-analysis. J Hepatol 72, 95–103. [PubMed: 31536748]

Comoglio PM, Trusolino L, and Boccaccio C (2018). Known and novel roles of the MET oncogene in cancer: a coherent approach to targeted therapy. Nat Rev Cancer 18, 341–358. [PubMed: 29674709]

Costa A, Kieffer Y, Scholer-Dahirel A, Pelon F, Bourachot B, Cardon M, Sirven P, Magagna I, Fuhrmann L, Bernard C, et al. (2018). Fibroblast Heterogeneity and Immunosuppressive Environment in Human Breast Cancer. Cancer Cell 33, 463–479 e410. [PubMed: 29455927]

Cyphert JM, Trempus CS, and Garantziotis S (2015). Size Matters: Molecular Weight Specificity of Hyaluronan Effects in Cell Biology. Int J Cell Biol 2015, 563818. [PubMed: 26448754]

Egeblad M, Rasch MG, and Weaver VM (2010). Dynamic interplay between the collagen scaffold and tumor evolution. Curr Opin Cell Biol 22, 697–706. [PubMed: 20822891]

Elyada E, Bolisetty M, Laise P, Flynn WF, Courtois ET, Burkhart RA, Teinor JA, Belleau P, Biffi G, Lucito MS, et al. (2019). Cross-Species Single-Cell Analysis of Pancreatic Ductal Adenocarcinoma Reveals Antigen-Presenting Cancer-Associated Fibroblasts. Cancer Discov 9, 1102–1123. [PubMed: 31197017]

Erez N, Truitt M, Olson P, Arron ST, and Hanahan D (2010). Cancer-Associated Fibroblasts Are Activated in Incipient Neoplasia to Orchestrate Tumor-Promoting Inflammation in an NF-kappaB-Dependent Manner. Cancer Cell 17, 135–147. [PubMed: 20138012]

Fan B, Malato Y, Calvisi DF, Naqvi S, Razumilava N, Ribback S, Gores GJ, Dombrowski F, Evert M, Chen X, and Willenbring H (2012). Cholangiocarcinomas can originate from hepatocytes in mice. J Clin Invest 122, 2911–2915. [PubMed: 22797301]

Friedman G, Levi-Galibov O, David E, Bornstein C, Giladi A, Dadiani M, Mayo A, Halperin C, Pevsner-Fischer M, Lavon H, et al. (2020). Cancer-associated fibroblast compositions change with breast cancer progression linking the ratio of S100A4+ and PDPN+ CAFs to clinical outcome. Nature Cancer 1, 692–708.

Friedman SL (2008). Hepatic stellate cells: protean, multifunctional, and enigmatic cells of the liver. Physiol Rev 88, 125–172. [PubMed: 18195085]

Hanahan D, and Coussens LM (2012). Accessories to the crime: functions of cells recruited to the tumor microenvironment. Cancer Cell 21, 309–322. [PubMed: 22439926]

Hosein AN, Huang H, Wang Z, Parmar K, Du W, Huang J, Maitra A, Olson E, Verma U, and Brekken RA (2019). Cellular heterogeneity during mouse pancreatic ductal adenocarcinoma progression at single-cell resolution. JCI Insight 5.

Huh CG, Factor VM, Sanchez A, Uchida K, Conner EA, and Thorgeirsson SS (2004). Hepatocyte growth factor/c-met signaling pathway is required for efficient liver regeneration and repair. Proc Natl Acad Sci U S A 101, 4477–4482. [PubMed: 15070743]

Ilicic T, Kim JK, Kolodziejczyk AA, Bagger FO, McCarthy DJ, Marioni JC, and Teichmann SA (2016). Classification of low quality cells from single-cell RNA-seq data. Genome Biol 17, 29. [PubMed: 26887813]

Kalluri R (2016). The biology and function of fibroblasts in cancer. Nat Rev Cancer 16, 582–598. [PubMed: 27550820]

Kononen J, Bubendorf L, Kallioniemi A, Barlund M, Schraml P, Leighton S, Torhorst J, Mihatsch MJ, Sauter G, and Kallioniemi OP (1998). Tissue microarrays for high-throughput molecular profiling of tumor specimens. Nat Med 4, 844–847. [PubMed: 9662379]

Krempen K, Grotkopp D, Hall K, Bache A, Gillan A, Rippe RA, Brenner DA, and Breindl M (1999). Far upstream regulatory elements enhance position-independent and uterus-specific expression of the murine alpha1(I) collagen promoter in transgenic mice. Gene Expr 8, 151–163. [PubMed: 10634317]

Levental KR, Yu H, Kass L, Lakins JN, Egeblad M, Erler JT, Fong SF, Csiszar K, Giaccia A, Weninger W, et al. (2009). Matrix crosslinking forces tumor progression by enhancing integrin signaling. Cell 139, 891–906. [PubMed: 19931152]

Liotta LA (1986). Tumor invasion and metastases--role of the extracellular matrix: Rhoads Memorial Award lecture. Cancer Res 46, 1–7. [PubMed: 2998604]

Lun AT, Bach K, and Marioni JC (2016). Pooling across cells to normalize single-cell RNA sequencing data with many zero counts. Genome Biol 17, 75. [PubMed: 27122128]

Ma L, Hernandez MO, Zhao Y, Mehta M, Tran B, Kelly M, Rae Z, Hernandez JM, Davis JL, Martin SP, et al. (2019). Tumor Cell Biodiversity Drives Microenvironmental Reprogramming in Liver Cancer. Cancer Cell 36, 418–430 e416. [PubMed: 31588021]

Marti P, Stein C, Blumer T, Abraham Y, Dill MT, Pikiolek M, Orsini V, Jurisic G, Megel P, Makowska Z, et al. (2015). YAP promotes proliferation, chemoresistance, and angiogenesis in human cholangiocarcinoma through TEAD transcription factors. Hepatology 62, 1497–1510. [PubMed: 26173433]

Matsumoto K, Li Y, Jakuba C, Sugiyama Y, Sayo T, Okuno M, Dealy CN, Toole BP, Takeda J, Yamaguchi Y, and Kosher RA (2009). Conditional inactivation of Has2 reveals a crucial role for hyaluronan in skeletal growth, patterning, chondrocyte maturation and joint formation in the developing limb. Development 136, 2825–2835. [PubMed: 19633173]

McCarthy JB, El-Ashry D, and Turley EA (2018). Hyaluronan, Cancer-Associated Fibroblasts and the Tumor Microenvironment in Malignant Progression. Front Cell Dev Biol 6, 48. [PubMed: 29868579]

McInnes LH, J. (2018). UMAP: uniform manifold approximation and projection for dimension reduction. https://arxivorg/abs/180203426

Mederacke I, Dapito DH, Affo S, Uchinami H, and Schwabe RF (2015). High-yield and high-purity isolation of hepatic stellate cells from normal and fibrotic mouse livers. Nat Protoc 10, 305–315. [PubMed: 25612230]

Mederacke I, Hsu CC, Troeger JS, Huebener P, Mu X, Dapito DH, Pradere JP, and Schwabe RF (2013). Fate tracing reveals hepatic stellate cells as dominant contributors to liver fibrosis independent of its aetiology. Nat Commun 4, 2823. [PubMed: 24264436]

Mertens JC, Fingas CD, Christensen JD, Smoot RL, Bronk SF, Werneburg NW, Gustafson MP, Dietz AB, Roberts LR, Sirica AE, and Gores GJ (2013). Therapeutic effects of deleting cancer-associated fibroblasts in cholangiocarcinoma. Cancer Res 73, 897–907. [PubMed: 23221385]

Michalopoulos GK, and DeFrances MC (1997). Liver regeneration. Science 276, 60–66. [PubMed: 9082986]

Mu X, Pradere JP, Affo S, Dapito DH, Friedman R, Lefkovitch JH, and Schwabe RF (2016). Epithelial Transforming Growth Factor-beta Signaling Does Not Contribute to Liver Fibrosis but Protects Mice From Cholangiocarcinoma. Gastroenterology 150, 720–733. [PubMed: 26627606]

Northey JJ, Przybyla L, and Weaver VM (2017). Tissue Force Programs Cell Fate and Tumor Aggression. Cancer Discov 7, 1224–1237. [PubMed: 29038232]

Ohlund D, Handly-Santana A, Biffi G, Elyada E, Almeida AS, Ponz-Sarvise M, Corbo V, Oni TE, Hearn SA, Lee EJ, et al. (2017). Distinct populations of inflammatory fibroblasts and myofibroblasts in pancreatic cancer. J Exp Med 214, 579–596. [PubMed: 28232471]

Oscar Franzén L.-M. G. a. J. L. M. B. r. (2019). PanglaoDB: a web server for exploration of mouse and human single-cell RNA sequencing data. Database 2019, 1–9.

Ozdemir BC, Pentcheva-Hoang T, Carstens JL, Zheng X, Wu CC, Simpson TR, Laklai H, Sugimoto H, Kahlert C, Novitskiy SV, et al. (2014). Depletion of carcinoma-associated fibroblasts and fibrosis induces immunosuppression and accelerates pancreas cancer with reduced survival. Cancer Cell 25, 719–734. [PubMed: 24856586]

Phaneuf D, Moscioni AD, LeClair C, Raper SE, and Wilson JM (2004). Generation of a mouse expressing a conditional knockout of the hepatocyte growth factor gene: demonstration of impaired liver regeneration. DNA Cell Biol 23, 592–603. [PubMed: 15383179]

Pradere JP, Kluwe J, De Minicis S, Jiao JJ, Gwak GY, Dapito DH, Jang MK, Guenther ND, Mederacke I, Friedman R, et al. (2013). Hepatic macrophages but not dendritic cells contribute to liver fibrosis by promoting the survival of activated hepatic stellate cells in mice. Hepatology 58, 1461–1473. [PubMed: 23553591]

Provenzano PP, Cuevas C, Chang AE, Goel VK, Von Hoff DD, and Hingorani SR (2012). Enzymatic targeting of the stroma ablates physical barriers to treatment of pancreatic ductal adenocarcinoma. Cancer Cell 21, 418–429. [PubMed: 22439937]

Ramanathan RK, McDonough SL, Philip PA, Hingorani SR, Lacy J, Kortmansky JS, Thumar J, Chiorean EG, Shields AF, Behl D, et al. (2019). Phase IB/II Randomized Study of FOLFIRINOX Plus Pegylated Recombinant Human Hyaluronidase Versus FOLFIRINOX Alone in Patients With Metastatic Pancreatic Adenocarcinoma: SWOG S1313. J Clin Oncol 37, 1062–1069. [PubMed: 30817250]

Raudvere U, Kolberg L, Kuzmin I, Arak T, Adler P, Peterson H, and Vilo J (2019). g:Profiler: a web server for functional enrichment analysis and conversions of gene lists (2019 update). Nucleic Acids Res 47, W191–W198. [PubMed: 31066453]

Reich M, Liefeld T, Gould J, Lerner J, Tamayo P, and Mesirov JP (2006). GenePattern 2.0. Nat Genet 38, 500–501. [PubMed: 16642009]

Reimand J, Isserlin R, Voisin V, Kucera M, Tannus-Lopes C, Rostamianfar A, Wadi L, Meyer M, Wong J, Xu C, et al. (2019). Pathway enrichment analysis and visualization of omics data using g:Profiler, GSEA, Cytoscape and EnrichmentMap. Nat Protoc 14, 482–517. [PubMed: 30664679]

Rhim AD, Oberstein PE, Thomas DH, Mirek ET, Palermo CF, Sastra SA, Dekleva EN, Saunders T, Becerra CP, Tattersall IW, et al. (2014). Stromal elements act to restrain, rather than support, pancreatic ductal adenocarcinoma. Cancer Cell 25, 735–747. [PubMed: 24856585]

Riener MO, Vogetseder A, Pestalozzi BC, Clavien PA, Probst-Hensch N, Kristiansen G, and Jochum W (2010). Cell adhesion molecules P-cadherin and CD24 are markers for carcinoma and dysplasia in the biliary tract. Hum Pathol 41, 1558–1565. [PubMed: 20621328]

Rizvi S, Fischbach SR, Bronk SF, Hirsova P, Krishnan A, Dhanasekaran R, Smadbeck JB, Smoot RL, Vasmatzis G, and Gores GJ (2018a). YAP-associated chromosomal instability and cholangiocarcinoma in mice. Oncotarget 9, 5892–5905. [PubMed: 29464042]

Rizvi S, Khan SA, Hallemeier CL, Kelley RK, and Gores GJ (2018b). Cholangiocarcinoma - evolving concepts and therapeutic strategies. Nat Rev Clin Oncol 15, 95–111. [PubMed: 28994423]

Rousseeuw PJ (1987). Silhouettes: a graphical aid to the interpretation and validation of cluster analysis. Journal of computational and applied mathematics 20 (1987): 53–65.

Sahai E, Astsaturov I, Cukierman E, DeNardo DG, Egeblad M, Evans RM, Fearon D, Greten FR, Hingorani SR, Hunter T, et al. (2020). A framework for advancing our understanding of cancer-associated fibroblasts. Nat Rev Cancer 20, 174–186. [PubMed: 31980749]

Seehawer M, Heinzmann F, D'Artista L, Harbig J, Roux PF, Hoenicke L, Dang H, Klotz S, Robinson L, Dore G, et al. (2018). Necroptosis microenvironment directs lineage commitment in liver cancer. Nature 562, 69–75. [PubMed: 30209397]

Senoo H, Mezaki Y, and Fujiwara M (2017). The stellate cell system (vitamin A-storing cell system). Anat Sci Int 92, 387–455. [PubMed: 28299597]

Sia D, Hoshida Y, Villanueva A, Roayaie S, Ferrer J, Tabak B, Peix J, Sole M, Tovar V, Alsinet C, et al. (2013). Integrative molecular analysis of intrahepatic cholangiocarcinoma reveals 2 classes that have different outcomes. Gastroenterology 144, 829–840. [PubMed: 23295441]

Sirica AE (2011). The role of cancer-associated myofibroblasts in intrahepatic cholangiocarcinoma. Nat Rev Gastroenterol Hepatol 9, 44–54. [PubMed: 22143274]

Stuart T, Butler A, Hoffman P, Hafemeister C, Papalexi E, Mauck WM 3rd, Hao Y, Stoeckius M, Smibert P, and Satija R (2019). Comprehensive Integration of Single-Cell Data. Cell 177, 1888–1902 e1821. [PubMed: 31178118]

Su S, Chen J, Yao H, Liu J, Yu S, Lao L, Wang M, Luo M, Xing Y, Chen F, et al. (2018). CD10(+)GPR77(+) Cancer-Associated Fibroblasts Promote Cancer Formation and Chemoresistance by Sustaining Cancer Stemness. Cell 172, 841–856 e816. [PubMed: 29395328]

Tian X, Azpurua J, Hine C, Vaidya A, Myakishev-Rempel M, Ablaeva J, Mao Z, Nevo E, Gorbunova V, and Seluanov A (2013). High-molecular-mass hyaluronan mediates the cancer resistance of the naked mole rat. Nature 499, 346–349. [PubMed: 23783513]

Toole BP (2004). Hyaluronan: from extracellular glue to pericellular cue. Nat Rev Cancer 4, 528–539. [PubMed: 15229478]

Vento-Tormo R, Efremova M, Botting RA, Turco MY, Vento-Tormo M, Meyer KB, Park JE, Stephenson E, Polanski K, Goncalves A, et al. (2018). Single-cell reconstruction of the early maternal-fetal interface in humans. Nature 563, 347–353. [PubMed: 30429548]

Wang J, Dong M, Xu Z, Song X, Zhang S, Qiao Y, Che L, Gordan J, Hu K, Liu Y, et al. (2018). Notch2 controls hepatocyte-derived cholangiocarcinoma formation in mice. Oncogene 37, 3229–3242. [PubMed: 29545603]

Wang J, Wang H, Peters M, Ding N, Ribback S, Utpatel K, Cigliano A, Dombrowski F, Xu M, Chen X, et al. (2019). Loss of Fbxw7 synergizes with activated Akt signaling to promote c-Myc dependent cholangiocarcinogenesis. J Hepatol 71, 742–752. [PubMed: 31195063]

Yang YM, Noureddin M, Liu C, Ohashi K, Kim SY, Ramnath D, Powell EE, Sweet MJ, Roh YS, Hsin IF, et al. (2019). Hyaluronan synthase 2-mediated hyaluronan production mediates Notch1 activation and liver fibrosis. Sci Transl Med 11.

Zhang M, Yang H, Wan L, Wang Z, Wang H, Ge C, Liu Y, Hao Y, Zhang D, Shi G, et al. (2020a). Single cell transcriptomic architecture and intercellular crosstalk of human intrahepatic cholangiocarcinoma. J Hepatol.

Zhang M, Yang H, Wan L, Wang Z, Wang H, Ge C, Liu Y, Hao Y, Zhang D, Shi G, et al. (2020b). Single-cell transcriptomic architecture and intercellular crosstalk of human intrahepatic cholangiocarcinoma. J Hepatol 73, 1118–1130. [PubMed: 32505533]

Highlights

- The majority of CAF in ICC are derived from hepatic stellate cells
- Inflammatory CAF promote ICC through HGF and its receptor MET
- myCAF promote ICC through Has2/hyaluronic acid
- CAF-derived type I collagen contributes to stiffness but does not promote ICC growth

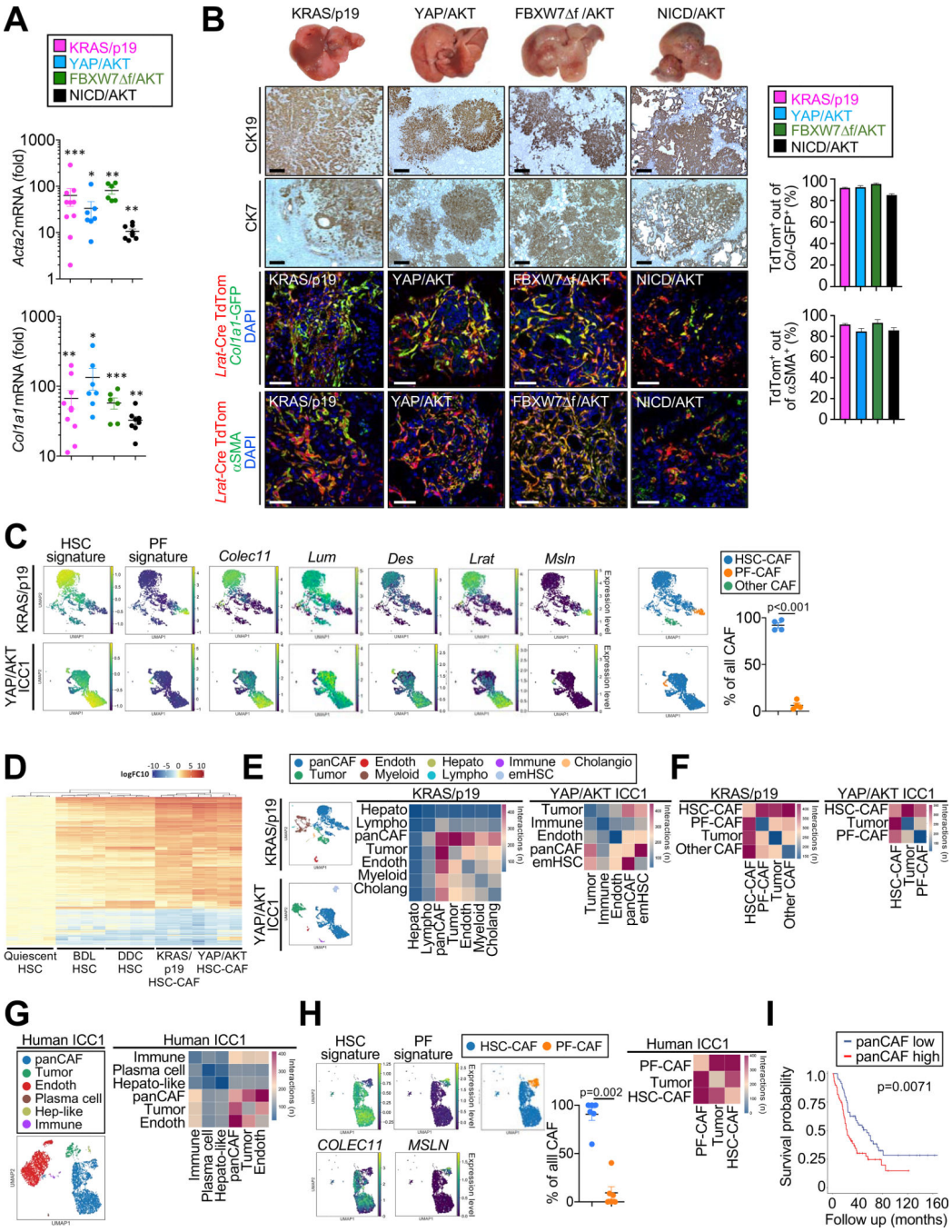

Figure 1 |.

The majority of CAF are HSC derived and closely interact with tumor cells in ICC. (A) Acta2 and Col1a1 mRNA expression in murine ICC. Data are shown as mean±SEM. Significance for each model was calculated by two-sided unpaired T-test or Mann-Whitney test vs its own control, *p<0.05; ** p<0.01; ***p<0.001. (B) Representative photographs, CK19 and CK7 IHC confocal microscopy and quantifications, showing colocalization of Lrat-Cre induced TdTom with CAF markers Col1a1-GFP and αSMA in four murine ICC models (n=3/model) in Lrat-Cre^{+} TdTom^{+}Col1a1-GFP^{+} mice. Scale bars, 50 μm. Data

shown as mean±SEM. (C) Representative UMAPs of scRNA-seq HSC and PF signature scores HSC markers Colec11, Lum, Des and Lrat, and PF marker Msln in KRAS/p19 (n=1) and YAP/AKT-induced ICC (n=3) and the percentage of CAF populations. (D) Heatmap of genes from bulk RNA-seq with > 2log fold change and p-value <0.01 in quiescent HSC (n=4), HSC from bile duct ligation (BDL) (n=4), HSC from 0.1% DDC diet (n=4), HSC-CAF from YAP/AKT (n=4) and KRAS/p19 (n=3) when compared to qHSC (n=4). (E,F) CellphoneDB analysis showing the number of ligand–receptor interactions between (E) all cell populations and (F) HSC-CAF and PF-CAF with tumor cells in KRAS/p19- and YAP/AKT-induced ICC. (G-H) Representative UMAPs and heatmaps of scRNA-seq showing (G) cell populations and the number of ligand–receptor interactions between all cells, (H) HSC and PF signature scores and percentage (n=6); and number of ligand–receptor interactions (n=5) in human ICC. Data shown as mean±SEM. Significance calculated by Mann-Whitney test. (I) Overall survival in 119 ICC patients with low (n=59) and high (n=60) panCAF signature.

See also Figure S1, Table S1, S2, S3.

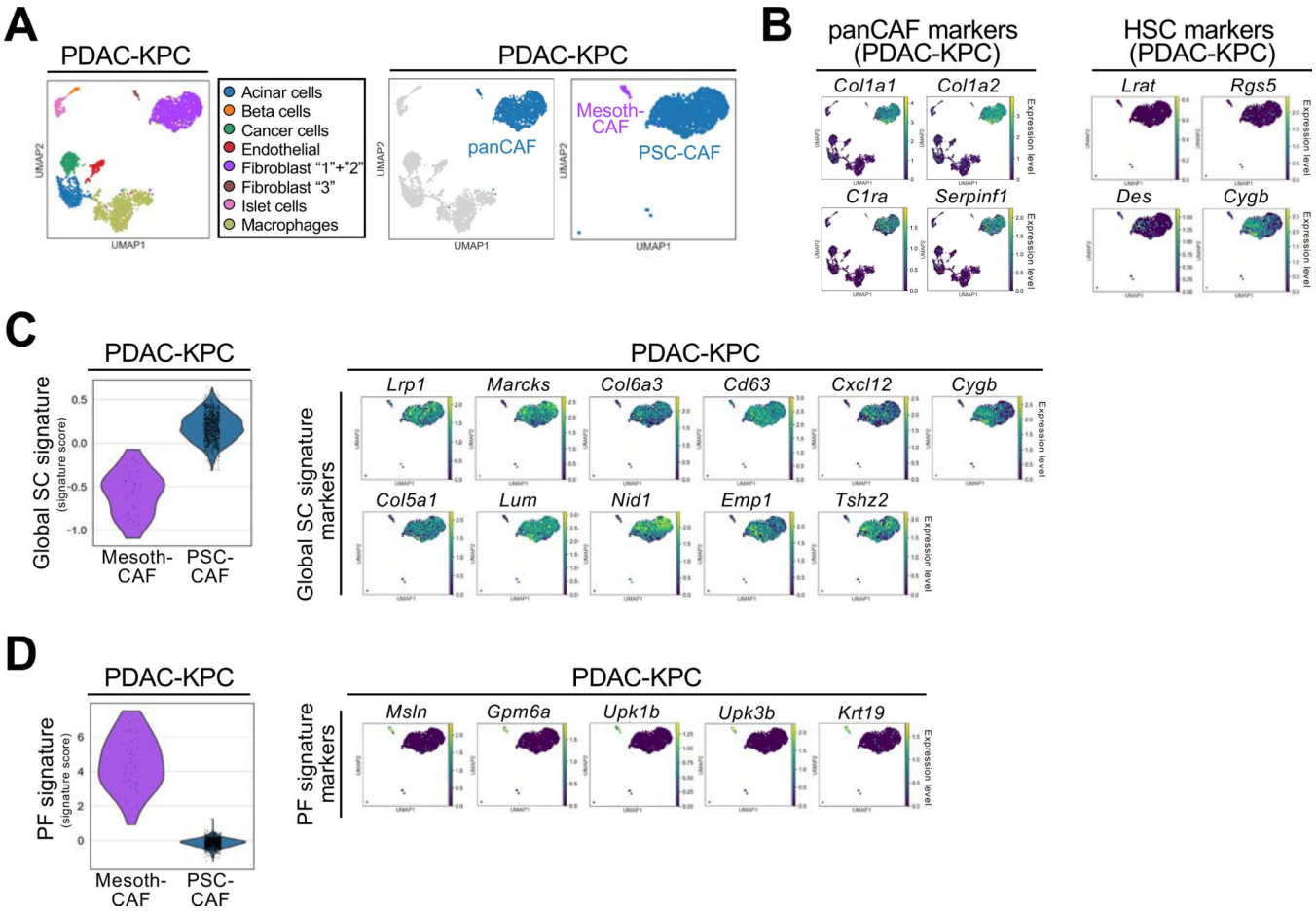

Figure 2 |.

Comparison of CAF from ICC and PDAC. (A) UMAPs showing cell populations detected by scRNA-seq in KPC-induced mouse PDAC from Hosein et al. (B) UMAPs showing the normalized expression levels of panCAF and HSC markers in PDAC-KPC. (C,D) Violin plot showing the global SC signature (C) and PF signature (D) scores and UMAPs for each gene of these signatures. For C,D, the width of each violin plot indicates the kernel density of the expression values.

See also Figure S2.

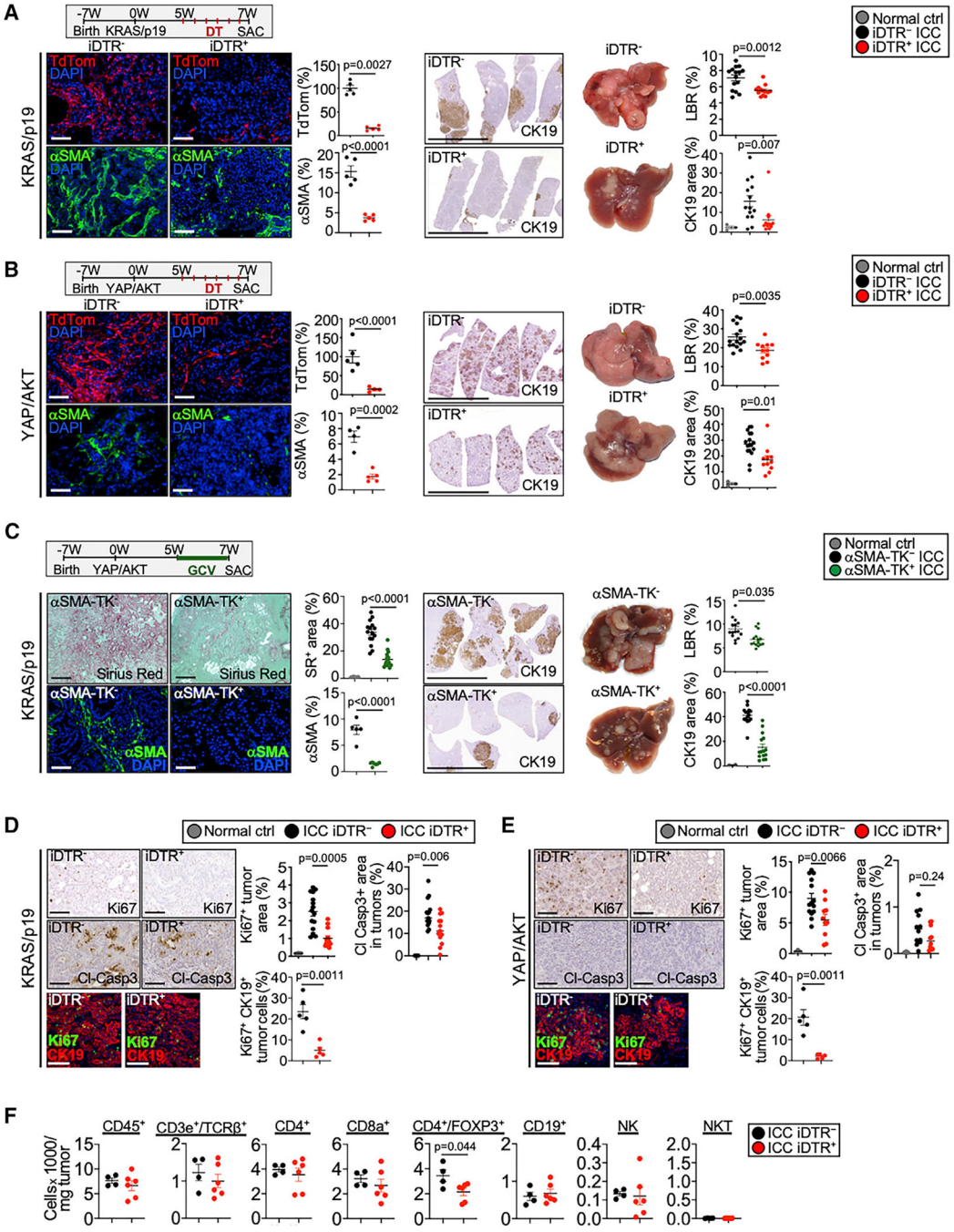

Figure 3. HSC-derived CAF promote ICC development and tumor cell proliferation

(A and B) HSC-derived CAF were depleted in mice with (A) KRAS/p19-induced and (B) YAP/AKT-induced ICC by injecting *Lrat*-Cre^{+}TdTom^{+}iDTR^{+} or *Lrat*-Cre^{+}TdTom^{+}iDTR^{-} littermates with diphtheria toxin. HSC depletion was quantified by the TdTom^{+} and αSMA^{+} area (n = 4–5 mice/group). Scale bars, 100 μm. Representative images of IHC and livers, liver/body weight ratio (LBR), and CK19^{+} quantifications from (A) KRAS/p19-induced ICC (n = 13–15 mice/group) and (B) YAP/AKT-induced ICC (n = 11–16 mice/group) show reduced ICC in HSC-CAF-depleted mice. Scale bars, 1 cm.

(C) CAF were depleted by injecting ganciclovir in αSMA-TK mice with KRAS/p19-induced ICC. CAF depletion was quantified by αSMA IHC (n = 5–7 mice/group) and Sirius red (n = 15 mice/group). Scale bars, 100 μm. Representative images of CK19 IHC, livers, LBR, and quantifications from KRAS/p19 ICC in αSMA-TK mice (n = 15 mice/group). Scale bars, 1 cm.

(D and E) Representative pictures and quantifications of Ki67 and cl-caspase3 IHC and confocal imaging and quantifications of $Ki67^{+}CK19^{+}$ cells in (D) KRAS/p19 and (E) YAP/AKT ICC in CAF-depleted $iDTR^{+}$ and control $iDTR^{-}$ mice. Scale bars, 100 μm.

(F) Flow cytometry of indicated immune cells in tumors from KRAS/p19 ICC in $iDTR^{-}$ (n = 4) and $iDTR^{+}$ (n = 6) mice.

Data shown as mean ± SEM. Significance determined by two-sided unpaired t test (groups of two) (A, B, D, F), by one-way ANOVA and Sidak's post hoc test (C, E: Ki67 panel), or by Kruskal-Wallis test with Dunn's post hoc test (A, B, D, E: Cl-Casp3 panel) (groups of three). See also Figure S3.

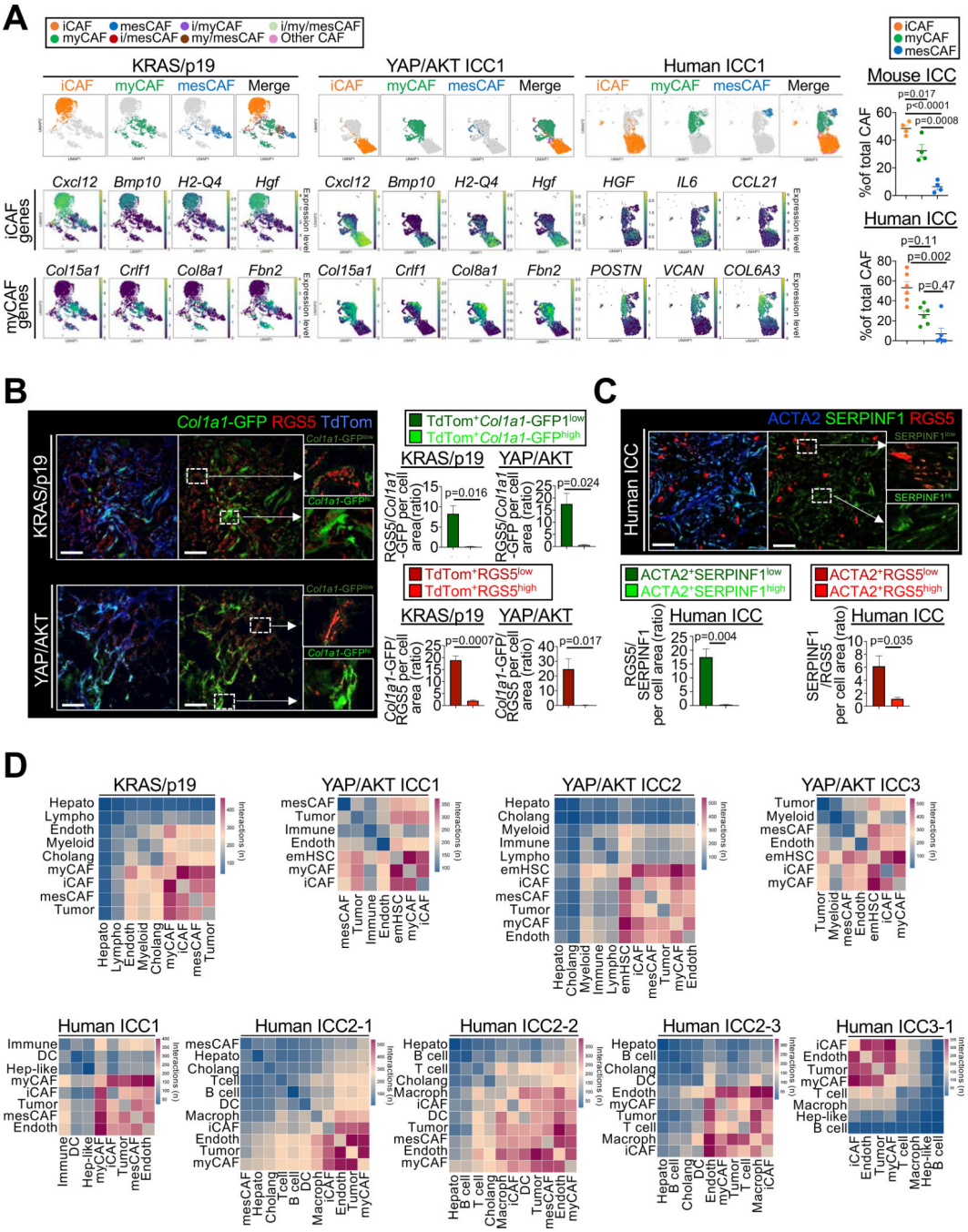

Figure 4 |.

CAF subpopulations and their ligand-receptor interactome in ICC. (A) Representative UMAPs of indicated genes, CAF subpopulations and their percentages in KRAS/p19 (n=1), YAP/AKT-induced (n=3) and human ICC (n=6). Data shown as mean±SEM, significance determined by one-way ANOVA followed by Sidak's posthoc test (mouse) or Kruskal-Wallis test with Dunn's posthoc test (human). (B) Representative confocal microscopy and quantifications show high RGS5 in Col1a1-GFP^{low} iCAF and low RGS5 in Col1a1-GFP^{high} myCAF in Lrat-Cre^{+} TdTom^{+}Col1a1-GFP^{+} mice (n=3 tumors/model). Scale bars, 50 μm.

Data shown as mean±SEM, significance determined by two-sided unpaired T-test. (C) Representative confocal microscopy and quantifications show high expression of iCAF marker RGS5 in cells with low expression of myCAF marker SERPINF1 and vice versa (n=3 tumors). Scale bars, 50 μm. Data shown as mean±SEM, and significance determined by two-sided unpaired T-test. (D) Representative heatmaps of CellphoneDB analysis showing the number of ligand–receptor interactions between iCAF, myCAF and mesCAF and all other cells in KRAS/p19 (n=1) and YAP/AKT ICC (n=3), and in human ICC (n=5). See also Figure S4, Table S4, S5.

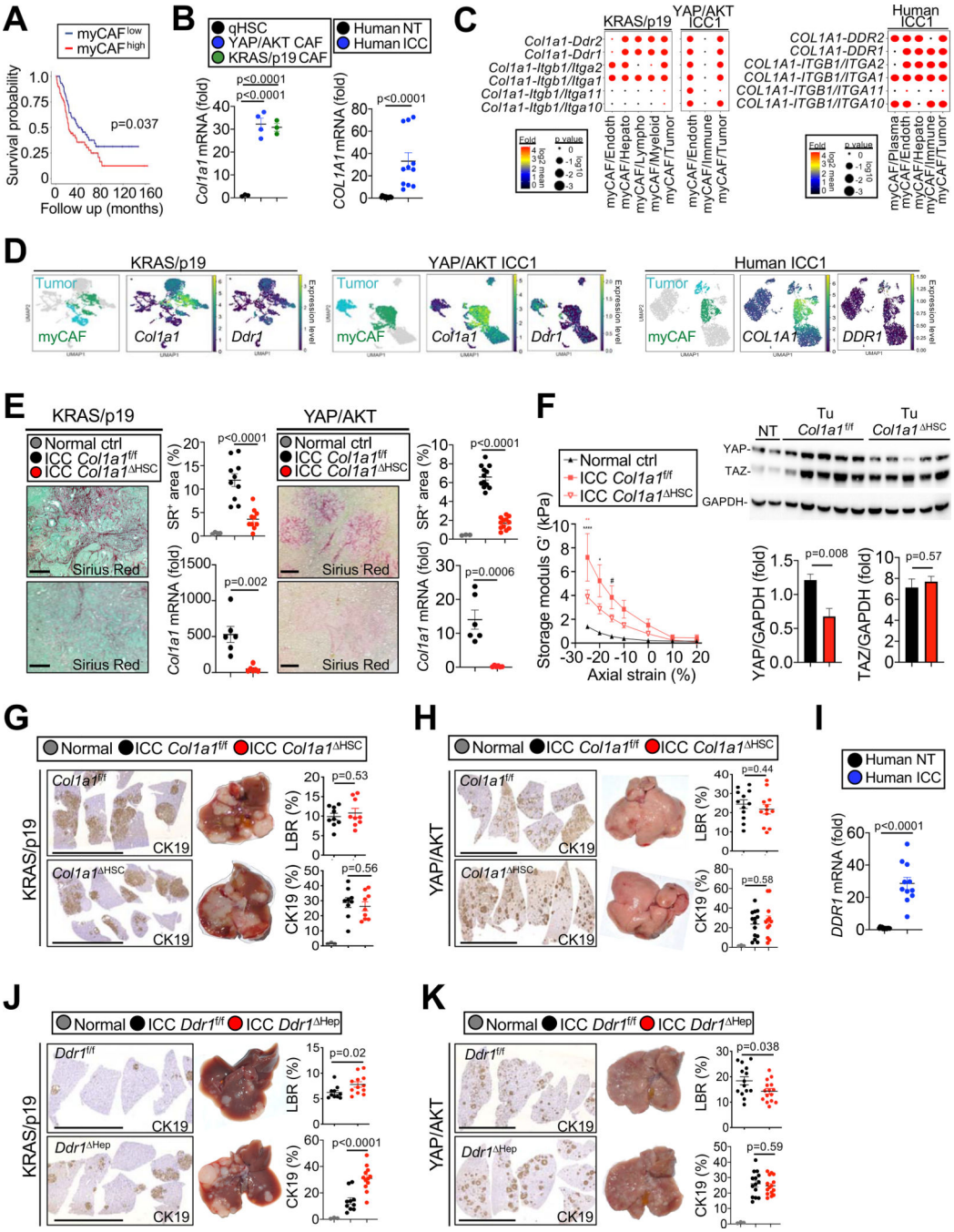

Figure 5 |.

Col1a1 affects tumor stiffness but not tumor growth in ICC. (A) Overall survival in 119 ICC patients with low (n=59) and high (n=60) myCAF signature. (B) Col1a1 mRNA in quiescent HSC (n=4) and HSC-derived CAF from KRAS/p19- (n=3) and YAP/AKT-(n=4) induced ICC and *COL1A1* mRNA expression in non-tumor (NT) and tumor (T) tissues (n=11) from ICC patients. (C) Ligand-receptor interactions between *COL1A1*-expressing myCAF and other cells in mouse and human ICC. (D) Representative UMAPs of indicated genes in KRAS/p19- and YAP/AKT- ICC, and human ICC. (E) Representative images and

quantification of sirius red staining and *Col1a1* qPCR in *Col1a1*$^{f/f}$ and *Col1a1*$^{\Delta HSC}$ KRAS/p19 ICC (n=9 each) and YAP/AKT ICC (n=12 each). Scale bars 100 μm. (F) Storage modulus G' (a measure of elasticity) in *Col1a1*$^{f/f}$ (n=3) and *Col1a1*$^{\Delta HSC}$ (n=4) mice in a KRAS/p19 ICC and in control liver (n=2) by shear rheometry. Curves are mean±SEM. Using 2-way ANOVA: *p≤0.05, **p≤0.01, ****p≤0.0001, #0.05<p≤0.10 vs ctrl (black) or vs *Col1a1*$^{\Delta HSC}$ (red). YAP and TAZ Western blot and quantifications normalized to GAPDH in *Col1a1*$^{f/f}$ and *Col1a1*$^{\Delta HSC}$ (NT n=1 each, T n=5 each). (G,H) Representative images of CK19 IHC, livers, LBR and quantifications from (G) KRAS/p19 ICC (n=9 mice/group) and (H) YAP/AKT ICC (n=12–13 mice/group) in *Col1a1*$^{f/f}$ and *Col1a1*$^{\Delta HSC}$. Scale bars 1 cm. (I) *DDR1* mRNA expression in NT and T (n=11 each) from ICC patients. (J,K) Representative images and quantifications of CK19 IHC, livers, LBR from (J) KRAS/p19 ICC (n=10–12 mice/group) and (K) YAP/AKT-induced ICC (n=12–14 mice/group) in *Ddr1*$^{f/f}$ and *Ddr1*$^{\Delta Hep}$ mice. Scale bars 1 cm. Data shown as mean±SEM, significance determined by two-sided unpaired T-test (E,F,G,H,I,K) or Mann-Whitney (B human,F,J) (groups of two); and by one-way ANOVA followed by Sidak's posthoc test (B mouse,F) (groups of three). See also Figure S5.

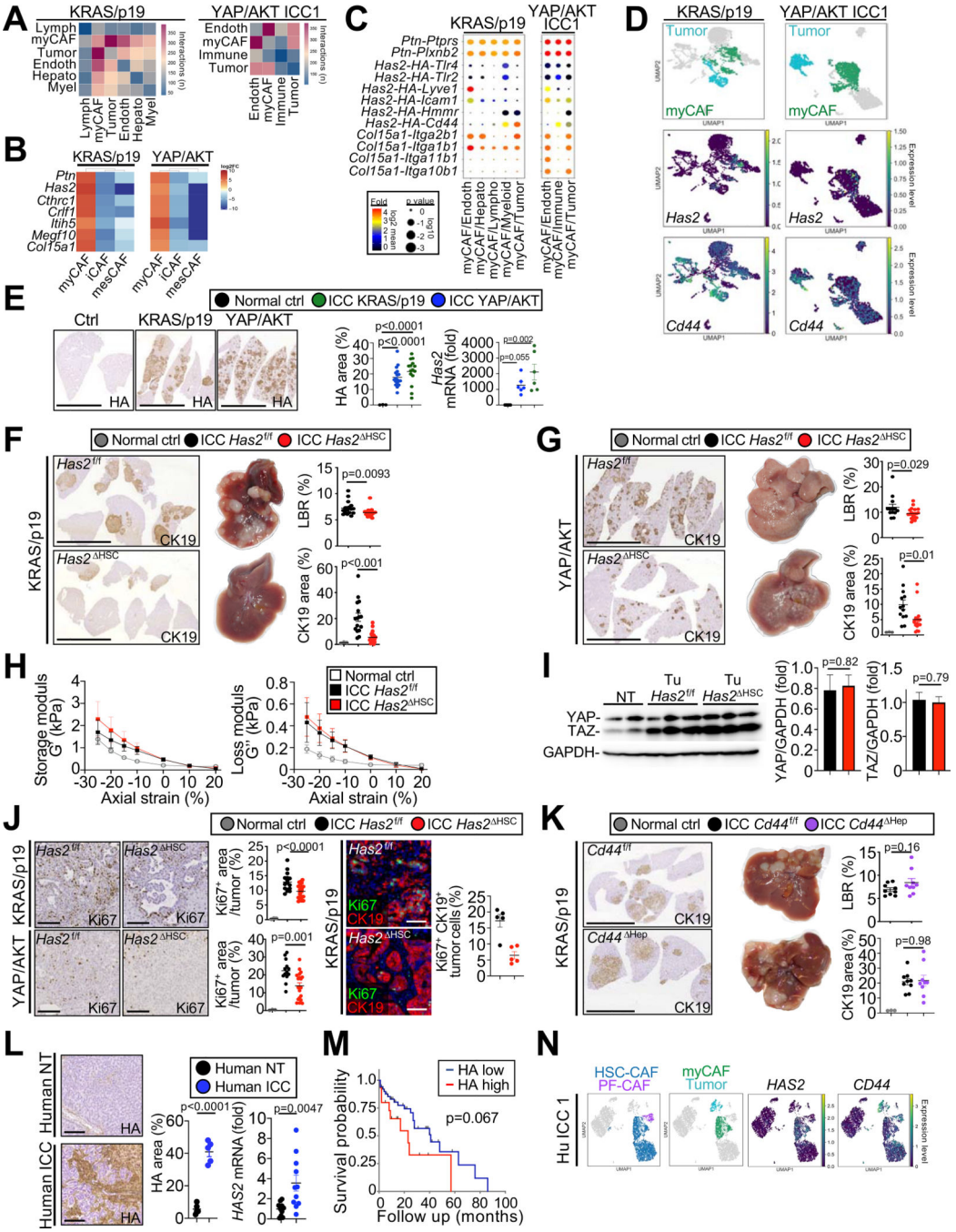

Figure 6 |. myCAF-derived HAS2 mediates tumor promotion.

(A) Representative CellphoneDB showing the number of interactions between myCAF and other cells in murine ICC. (B) Heatmap of genes differentially expressed in myCAF vs iCAF and mesCAF in KRAS/p19 and YAP/AKT ICC. (C) Representative CellphoneDB ligand–receptor pairs linking myCAF to other cells. (D) Representative UMAPs of indicated genes in KRAS/p19 and YAP/AKT ICC. (E) Representative micrographs and quantifications of HA IHC and Has2 mRNA in livers of KRAS/p19 ICC (n=9–15), YAP/AKT ICC (n=16) and control mice (n=3–4). Scale bars 1 cm. (F,G) Representative images of CK19 IHC,

livers, LBR and CK19^{+} area from KRAS/p19 ICC (n=16–20 mice/group) and YAP/AKT ICC (n=13–19 mice/group) in Has2$^{f/f}$ and Has2$^{\Delta HSC}$ mice. Scale bars 1 cm. (H) Storage modulus G' (a measure of elasticity) and loss modulus G" (a measure of viscosity) in tumors from Has2$^{f/f}$ and Has2$^{\Delta HSC}$ mice (n=4 each) in KRAS/p19 ICC and control liver (n=2) by shear rheometry. Curves are mean±SEM. Using 2-way ANOVA: *p≤0.05, **p≤0.01, ****p≤0.0001, #0.05<p≤0.10 vs ctrl (black) or vs Has2$^{\Delta HSC}$ (red). (I) YAP and TAZ western blot and quantifications normalized to GAPDH in Has2$^{f/f}$ and Has2$^{\Delta HSC}$ mice (NT n=1, T n=3 each). (J) Representative Ki67 IHC from KRAS/p19 (n=16–20 mice/group) and YAP/AKT ICC (n=13–19 mice/group) and Ki67-CK19 costaining, confocal microscopy and quantification (n=5/group) in Has2$^{f/f}$ and Has2$^{\Delta HSC}$ mice. Scale bars 100 μm. (K) Representative images of CK19 IHC, livers, LBR and CK19^{+} area from Cd44$^{f/f}$ (n=9) and Cd44$^{\Delta hep}$ (n=9) in KRAS/p19-induced ICC. Scale bars 1 cm. (L) Representative pictures and quantifications of HA IHC and HAS2 mRNA in human ICC (n=5) and matching non-tumor (n=5). Scale bars 100 μm. (M) Survival of CCA patients with low (n=50) or high (n=16) HA expression. (N) Representative UMAPs of HAS2 and CD44 in human ICC. Data shown as mean ±SEM (E-L). Significance determined by two-sided unpaired T-test (J,K) or Mann-Whitney (F,G) (groups of two); and by one-way ANOVA followed by Sidak's posthoc test (E,G,J) or Kruskal-Wallis with Dunn's posthoc (F,G) (groups of three).
See also Figure S6, Table S6.

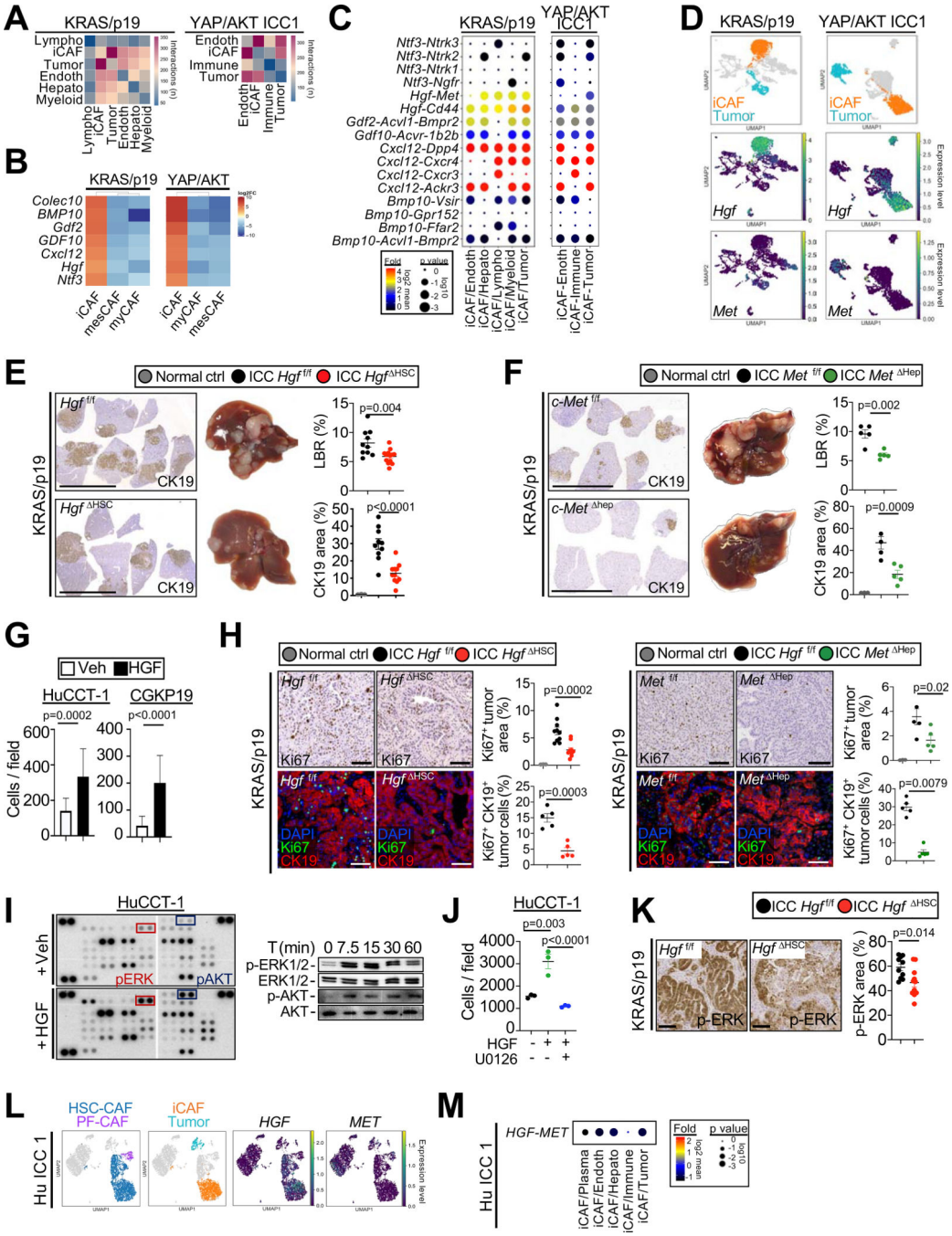

Figure 7 |. iCAF-derived HGF promotes ICC development and proliferation.

(A) Number of ligand–receptor interactions between iCAF and other cells in ICC. (B) Heatmap of genes differentially expressed in iCAF vs myCAF and mesCAF in KRAS/p19 and YAP/AKT ICC. (C) Ligand–receptor pairs linking iCAF to other cells shown as log2 mean. (D) Representative UMAPs of *Hgf and* Met in KRAS/p19 and YAP/AKT ICC. (E,F) Representative images of CK19 IHC, livers, LBR and CK19^{+} area from (E) *Hgf*$^{f/f}$ and *Hgf*$^{\Delta HSC}$ liver (n=10–11) and (F) *c-Met*$^{f/f}$ and *c-Met*$^{\Delta Hep}$ liver (n=5 each) in KRAS/p19 ICC. Scale bars 1 cm. (G) Cell counts of ICC cells lines after HGF or vehicle treatment (n=5

each) for 48h. (H) Representative Ki67 IHC in *Hgf*$^{f/f}$ and *Hgf*$^{\Delta HSC}$ (n=10–11) and *c-Met*$^{f/f}$ and *c-Met*$^{\Delta Hep}$ livers (n=5 each) mice and Ki67-CK19 costaining, confocal and quantification (n=5/group) in KRAS/p19-induced ICC. Scale bars 100 μm. (I) Phospho-kinase array and western blot for phospho and total ERK1/2 and AKT in HGF-treated HuCCT-1 cells. (J) Number of HuCCT-1 cells treated with HGF or vehicle for 48h, in the presence of MEK1/2 inhibitor U0126 or vehicle. (K) Phospho-ERK1/2 IHC and quantifications in KRAS/p19 ICC from *Hgf*$^{f/f}$ and *Hgf*$^{\Delta HSC}$ mice (n=10–11). (L) Representative UMAPs of *HGF* and *MET* in human ICC. (M) *HGF-MET* interactions linking iCAF to other populations in CellPhoneDB in one representative human ICC sample. For panels E-H,J,K data are shown as mean ±SEM. Significance determined by two-sided unpaired T-test (E-G:CGKP19 panel,K) or Mann-Whitney (G:HUCCT1 panel) (groups of two) or ANOVA test followed by Sidak's posthoc test (E,F,H,J) (groups of three).
See also Figure S7.

Table 1.

Correlation between human panCAF and myCAF signatures with clinicopathological parameters in a human cohort of 119 ICC patients

	panCAF low	panCAF high	Total	p value	myCAF low	myCAF high	Total	p value
n (%)	59	60	119		59	60	119	
Molecular class								
Proliferation class	18 (31)	54 (90)	72 (60)	**0.0001**	20 (34)	52 (87)	72 (60)	**0.0001**
Inflammation class	41 (69	6 (10)	47 (40)		39 (66)	8 (13)	47 (40)	
Demographics								
Sex, n (%)								
Male	28 (47)	37 (62)	65 (55)	0.142	29 (49)	36 (60)	65 (55)	0.272
Age, years								
Median (IQR)	62 (54–70)	64 (55–70)	64 (54–70)	0.91	62 (53–71)	64 (56–69)	64 (54–70)	0.901
Race, n (%)								
Caucasian	56 (96)	52 (86)	108 (92)	0.178	56 (97)	52 (87)	108 (92)	**0.018**
African American	1 (2)	1 (2)	2 (2)		2 (3)	0 (0)	2 (2)	
Asian	0 (0)	3 (5)	3 (3)		0 (0)	3 (5)	3 (2)	
Other	1 (2)	4 (7)	5 (3)		0 (0)	5 (8)	5 (4)	
Viral hepatitis, n (%)								
Hepatitis C	11 of 57 (19)	8 of 60 (13)	19 (16)	0.267	12 (21)	7 (12)	19 (16)	0.219
Hepatitis B	5 (9)	6 (10)	11 (9)	1	7 (12)	4 (7)	11 (9)	0.362
Cirrhosis, n (%)	8 (15)	12 (23)	20 (19)	0.331	8 (15)	12 (20)	20 (19)	0.458
Total bilirubin, n (%)								
>1 mg/dL	14 (25)	10 (18)	24 (21)	0.492	13 (24)	11 (19)	24 (21)	0.648
Serum ALT, n (%)								
>40 IU/L	12 (21)	19 (33)	31 (27)	0.206	12 (21)	19 (33)	31 (27)	0.209
Tumor features (pathologic)								
Tumor diameter, cm								
Median (IQR)	6 (4–9)	7 (5–9)	6 (4–9)	0.096	6 (4–8)	7 (5–11)	6 (4–9)	0.095
Tumor number, n (%)								
Single	47 (80)	52 (87)	99 (83)	0.337	48 (81)	51 (85)	99 (83)	0.632
Multiple	12 (20)	8 (13)	20 (17)		11 (19)	9 (15)	20 (17)	
Cell differentiation, n (%)								

	panCAF low	panCAF high	Total	p value	myCAF low	myCAF high	Total	p value
Well	14 (30)	4 (8)	18 (19)	**0.009**	11 (24)	7 (14)	18 (19)	0.298
Moderate-poor	33 (70)	44 (92)	77 (81)		35 (76)	42 (86)	77 (81)	
Stage[a], n (%)								
I + II	36 (62)	34 (57)	58 (49)	0.579	38 (64)	32 (54)	70 (59)	0.349
III + IV	22 (38)	26 (43)			21 (36)	27 (46)	48 (41)	
Macrovascular invasion, n (%)	4 (7)	12 (20)	16 (13)	**0.058**	4 (3)	12 (20)	24 (20)	**0.058**
Invasion of peritoneum, n (%)	0 (0)	4 (7)	4 (3)	0.119	0 (0)	4 (7)	4 (3)	0.119
Infiltration of resection margins, n (%)	22 (37)	32 (53)	54 (45)	0.1	21 (36)	33 (55)	54 (45)	0.09
Invasion of bile duct, n (%)	1 (2)	5 (8)	6 (5)	0.207	1 (2)	5 (83)	6 (5)	0.207
Intraneural invasion, n (%)	4 (7)	16 (27)	20 (17)	**0.006**	4 (7)	16 (27)	20 (17)	**0.006**
Satellites, n (%)	14 (24)	15 (25)	29 (24)	0.837	15 (25)	17 (28)	32 (27)	0.837

Variables included here have less than 10% of missing values except for cell differentiation (n = 24, 20% missing). IQR, interquartile range. p values in boldface are significant.

[a]Data according to the AJCC TNM stage, 7th edition.

KEY RESOURCES TABLE

REAGENT or RESOURCE	SOURCE	IDENTIFIER
Antibodies		
Rabbit Monoclonal anti-Phospho-p44/42 MAPK (Erk1/2) (Thr202/Tyr204) XP®	Cell Signaling	Cat: #4370; RRID: AB_2315112
Rabbit Monoclonal anti-p44/42 MAPK (Erk1/2) (137F5)	Cell Signaling	Cat: #4695; RRID: AB_390779
Rabbit Monoclonal anti-Phospho-Akt (Ser473) (D9E) XP®	Cell Signaling	Cat: #4060; RRID: AB_2315049
Rabbit polyclonal anti-Akt	Cell Signaling	Cat: #9272; RRID: AB_329827
Rabbit Monoclonal anti-YAP/TAZ (D24E4)	Cell Signaling	Cat: #8418; RRID: AB_10950494
Rabbit Monoclonal anti-DDR1 (D1G6) XP®	Cell Signaling	Cat: #5583; RRID: N/A
Goat anti-rabbit IgG-HRP	Santa Cruz	Cat: #sc-2004; RRID: AB_631746
Mouse Monoclonal anti-GAPDH-Peroxidase	Sigma	Cat: #G9295; RRID: AB_1078992
Rabbit monoclonal anti-Cytokeratin 19	Abcam	Cat: #ab133496; RRID: AB_11155282
Rabbit Polyclonal anti-Cytokeratin 7	Thermo Fisher Scientific	Cat: # 15539-1-AP, RRID: AB_2249769
Rabbit Monoclonal Recombinant Anti-Ki67 antibody [SP6]	Abcam	Cat: # ab16667; RRID: AB_302459
Rat Monoclonal anti-Ki-67 (SolA15), eBioscience™	Thermo Fisher Scientific	Cat: # 14569880; RRID: AB_10853185
Rabbit Polyclonal anti-Cleaved Caspase-3 (Asp175)	Cell Signaling	Cat: # 9661; RRID: AB_2341188
Rabbit monoclonal anti-CD3 [SP7]	Abcam	Cat: # ab16669; RRID: AB_443425
Mouse Monoclonal Anti-Actin, α-Smooth Muscle - FITC	Sigma	Cat: # F3777; RRID: AB_476977
Mouse Monoclonal Anti-Smooth muscle actin (clone BS66)	Nordic Biosite	Cat: # BSH-7459
Rabbit Polyclonal anti-RGS5	Abcam	Cat: # ab196799
Goat Polyclonal anti-SerpinF1/PEDF	R&D	Cat# AF1177; RRID: AB_2187173
Donkey Polyclonal anti-rabbit Alexa Fluor 488	Life Technologies	Cat: # A21206; RRID: AB_2535792
Donkey Polyclonal anti-mouse Alexa Fluor 488	Life Technologies	Cat: # A21202; RRID: AB_141607
Streptavidin, Alexa Fluor 594	Life Technologies	Cat: # S11227;
Streptavidin, Alexa Fluor 647	Life Technologies	Cat: # S21374; RRID: AB_2336066
Rat Monoclonal BUV395 Rat Anti-Mouse CD45 Clone 30-F11	BD Biosciences	Cat: #564279; RRID: AB_2651134
Rat Monoclonal BUV496 Anti-Mouse CD45R/B220 (clone RA3-6B2)	BD Biosciences	Cat: #564662; RRID: AB_2722578
Armenian Hamster Monoclonal BUV737 Anti-Mouse CD11c (clone HL3)	BD Biosciences	Cat: #564986; RRID: AB_2739034
Rat Monoclonal Brilliant Violet 510™ anti-mouse/human CD11b Antibody (clone M1/70)	BioLegend	Cat: #101263; RRID: AB_2629529
Armenian Hamster Monoclonal Brilliant Violet 711™ anti-mouse CD103 (clone 2B8)	BioLegend	Cat: #121435, RRID: AB_2686970
Rat Monoclonal PerCP-Cyanine5.5 Anti-Mouse CD19 (clone 1D3)	Tonbo biosciences	Cat: #65-0193; RRID: AB_2621887
Rat Monoclonal violetFluor™ 450 Anti-Mouse MHC Class II (I-A/I-E) (clone M5/114.15.2)	Tonbo biosciences	Cat: #75-5321; RRID: AB_2621965
Mouse Monoclonal PE/Cyanine7 anti-mouse CD64 (FcγRI) (clone X54-5/7.1)	BioLegend	Cat: #139314; RRID: AB_2563904
Rat Monoclonal APC Anti-Mouse F4/80 Antigen (clone BM8.1)	Tonbo biosciences	Cat: #20-4801; RRID: AB_2621602
Ghost Dye™ Red 780	Tonbo biosciences	Cat: #13-0865

REAGENT or RESOURCE	SOURCE	IDENTIFIER
Mouse Monoclonal BUV395 Anti-Mouse NK-1.1 Clone PK136	BD Biosciences	Cat: # 564144; RRID: AB_2738618
Mouse Monoclonal BUV496 Anti-Human CD3 Clone UCHT1	BD Biosciences	Cat: #564809; RRID: AB_2744388
Rat Monoclonal BUV737 Anti-Mouse CD4, clone RM4-5	BD Biosciences	Cat# 564933; RRID: AB_2732918
Rat Monoclonal anti-FOXP3 (FJK-16s), eFluor 450, eBioscience™	ThermoFisher Scientific	Cat: #48-5773-80; RRID: AB_1518813
Mouse Monoclonal Brilliant Violet 510™ anti-human CD45, clone HI30	BioLegend	Cat: #304036; RRID: AB_2561940
Armenian Hamster Monoclonal BV711 Anti-Mouse TCR β Chain, clone H57-597	BD Biosciences	Cat: #563135; RRID: AB_2738023
Armenian Hamster Monoclonal BV786 Anti-Mouse CD69, clone H1.2F3	BD Biosciences	Cat: #564683; RRID: AB_2738890
Rat Monoclonal PerCP-Cyanine5.5 anti-Mouse CD19, clone 1D3	Tonbo biosciences	Cat: #65-0193; RRID: AB_2621887
Rat Monoclonal APC anti-Mouse CD8a (53-6.7), clone 53-6.7	Tonbo biosciences	Cat: #20-0081; RRID: AB_2621550
Rat Monoclonal anti-Mouse CD44, Alexa Fluor®488, clone KM81	Cedarlane	Cat: #CL8944AF4
Rat IgG2a Isotype Control	ThermoFisher Scientific	Cat: # 02-9688; RRID: AB_2532970
Bacterial and virus strains		
AAV.TBG.PI.Cre.rBG (AAV8)	Addgene	Cat: Addgene#107787-AAV8
pAAV.TBG.PI.Null.bGH (AAV8)	Addgene	Cat: Addgene#105536-AAV8
Biological samples		
Human hilar cholangiocarcinoma	Columbia University, New York, NY	IRB- AAAN7562
Human intrahepatic cholangiocarcinoma tissue for RNA and IHC	Columbia University, New York, NY	IRB- AAAN2452-M01Y06
Human tissue microarrays	University Hospital Zurich, CH	Ethic committee: PB_2018_00252
Chemicals, peptides, and recombinant proteins		
Recombinant Mouse HGF Protein	R&D	Cat: #2207-HG
Recombinant Human HGF Protein	R&D	Cat: #294-HG
Recombinant Human Aggrecan aa20-675/His, biotin	R&D	CUSTOM-Protein
U-0126 ERK-inhibitor	Cayman Chemical	Cat: #70970
Hyaluronidase from bovine testes Type IV-S	Millipore Sigma	Cat: #H4272
Hyaluronan (High MW)	R&D	Cat: # GLR002
Hyaluronan (Medium MW)	R&D	Cat: # GLR004
Hyaluronan (Low MW)	R&D	Cat: #GLR001
Hyaluronic acid sodium salt from rooster comb	Millipore Sigma	Cat: # H5388
HEALON® PRO OVD	Johnson and Johnson vision	
Hyaluronic acid potassium salt - from Cockscomb	Carbosynth	Cat: #31799-91-4
DMEM - Dulbecco's Modified Eagle Medium	ThermoFisher Scientific	Cat: #11965118
DMEM, high glucose, HEPES, no phenol red	ThermoFisher Scientific	Cat: # 21063029
Foundation Fetal Bovine Serum	GeminiBio	Cat: # 900-108
Trypsin-EDTA (0.25%), phenol red	ThermoFisher Scientific	Cat: # 25200056
Gentamicin	ThermoFisher Scientific	Cat: #15710072

REAGENT or RESOURCE	SOURCE	IDENTIFIER
Penicillin-Streptomycin-Glutamine	ThermoFisher Scientific	Cat: # 10378016
Protease from Streptomyces griseus Type XIV	Millipore Sigma	Cat: #P5147-5G
Collagenase D from Clostridium histolyticum	Millipore Sigma	Cat: #11088882001
DNase I grade II, from bovine pancreas	Millipore Sigma	Cat: # 10104159001
Gey's Balanced Salt Solution	Millipore Sigma	Cat: #G9779
Percoll pH 8.5–9.5	Millipore Sigma	Cat: #P4937
Collagenase A from Clostridium histolyticum	Millipore Sigma	Cat: #10103578001
RPMI 1640	ThermoFisher Scientific	Cat: #11835030
Nycodenz	Cosmobio	Cat: #1002424
PhosSTOP	Millipore Sigma	Cat: #4906845001
cOmplete™, Mini Protease Inhibitor Cocktail	Millipore Sigma	Cat: #11836153001
Amersham™ Protran® Western blotting membranes, nitrocellulose	Millipore Sigma	Cat: # GE10600006
Restore™ Western Blot Stripping Buffer	ThermoFisher Scientific	Cat: #21059
RIPA buffer	Fisher Scientific	Cat: #R3792
QuantaBlu™ Fluorogenic Peroxidase Substrate Kit	ThermoFisher Scientific	Cat: #15169
TRIzol™ Reagent	ThermoFisher Scientific	Cat#15596018
Ganciclovir	Invivogen	Cat: # sud-gcv
Diphtheria Toxin from Corynebacterium diphtheriae	Millipore Sigma	Cat: #D0564
Poly (I:C)	GE Healthcare	Cat: #27473201
SoftSubstrates plates, rigidity 2kPa, 16kPa, 64kPa	SoftSubstrates, MuWells	Cat: # 2kPa-6W; #16kPa-6W; #64kPa-6W
High binding BINDING 96 WELL PLATES, STERILE	Greiner BIO-ONE	Cat: # 655077
Opal 520 Reagent	Perkin Elmer	Cat: # FP1487001KT
Opal 690 Reagent	Perkin Elmer	Cat: # FP1488001KT
Critical commercial assays		
Proteome Profiler Human Phospho-Kinase Array Kit	R&D	Cat: #ARY003B
RNeasy Micro Kit	Qiagen	Cat: #74004
Hyaluronan ELISA Duo set	R&D	Cat: #DY3614
Mouse HGF DuoSet ELISA	R&D	Cat: #DY2207
SuperSignal™ West Femto Maximum Sensitivity Substrate	ThermoFisher Scientific	Cat: #32106
Vectastatin Elite ABC-HRP kit	Vector Laboratories	Cat: #PK-6100; RRID: AB_2336819
DAB Peroxidase (HRP) Substrate Kit (with Nickel), 3,3'-diaminobenzidine	Vector Laboratories	Cat: #SK-4100; RRID: AB_2336382
BrdU Cell Proliferation Kit	Millipore Sigma	Cat: #2752
Quant-iT PicoGreen dsDNA Assay Kit	ThermoFisher Scientific	Cat: #P11496
Multi Tissue Dissociation Kit 1	Miltenyi Biotec	Cat: #130-110-201
Chromium Single Cell 3' Reagent Kits v2	10x Genomics	Cat: #PN-120237
Chromium Single Cell 3' Reagent Kits v3	10x Genomics	Cat: #PN-1000268
RNAscope® Multiplex Fluorescent Reagent Kit v2	Advanced Cell Diagnostic	Cat: #323100
Deposited data		

REAGENT or RESOURCE	SOURCE	IDENTIFIER
Bulk RNA-seq data	This Paper	GEO: GSE154170
scRNA-seq data	This Paper	GEO: GSE154170
Human intrahepatic cholangiocarcinoma	Zhang et al; J Hepatol, 2020. PMID: 32505533	GEO: GSE142784
Human intrahepatic cholangiocarcinoma	Ma et al.; Cancer Cell, 2019. PMID: 31588021	GEO: GSE125449
Human intrahepatic cholangiocarcinoma microarray	Sia *et* al.; Gastroenterology, 2013. PMID: 23295441	GEO: GSE32225
Mouse model of pancreatic ductal adenocarcinoma	Hosein et al.; JCI Insight, 2019. PMID: 31335328	GEO: GSE125588
Experimental models: cell lines		
Human: HuCCT-1	from Dr. Gregory Gores	RRID: CVCL_0324
Human: MzChA-1	from Dr. Gregory Gores	RRID: CVCL_6932
Mouse: SB1	from Dr. Gregory Gores	Rizvi *et al;* Oncotarget, 2018. PMID: 29464042
Mouse: CGKP19	This Paper	N/A
Experimental models: organisms/strains		
Mouse: C57BL/6J, *TdTomato* Ai14 reporter	Jackson Laboratory	Stock number: #007914
Mouse: *Rosa26*-iDTR (iDTR)	Jackson Laboratory	Stock number: #007900
Mouse: *Mx1*-Cre	Jackson Laboratory	Stock number: #003556
Mouse: *Rag2* KO	Jackson Laboratory	Stock number: #008449
Mouse: *Ddr1*^{tm1a}	Infrafrontier/EMMA	EM:09692
Mouse: *Col1a1*-GFP reporter	From Dr. David Brenner	MGI:4458034
Mouse: *Lrat*-Cre	Mederacke *et al*; Nat Commun, 2013. PMID:24264436	N/A
Mouse: αSMA-TK	From Dr. Raghu Kalluri	Jackson Laboratory Stock number: # 031155
Mouse: *Col1a1*$^{fl/fl}$	From Dr. Matthias Mack; Buchtler et al.; JASN, 2018. PMID: 29777019	N/A
Mouse: *Hgf*$^{fl/fl}$	From Dr. GK. Michalopoulos; Phaneuf et al.; DNA Cell Biol., 2004. PMID: 15383179	N/A
Mouse: *Lrat*-Cre *Has2*$^{fl/fl}$	From Dr. Ekihiro Seki, Yang et al.; Sci Transl Med., 2019. PMID: 31189722	N/A
Mouse: αSMA-*HAS2*Tg	From Dr. Ekihiro Seki, Yang et al.; Sci Transl Med., 2019. PMID: 31189722	N/A
Mouse: *Met*$^{fl/fl}$	From Dr. GK. Michalopoulos; Huh et al.; PNAS, 2004. PMID: 15070743	N/A
Mouse: *Cd44*$^{fl/fl}$	From Dr. E. Puré	N/A
Mouse: *RelA*$^{fl/fl}$	From Dr. R.M. Schmid; Algul et al.; JCI, 2007. PMID: 17525802	N/A

REAGENT or RESOURCE	SOURCE	IDENTIFIER
Oligonucleotides		
RNAscope® Probe - Mm-*Has2*-C2	Advanced Cell Diagnostic	Cat: #465171-C2
RNAscope® Probe - Mm-*Hgf*-C3	Advanced Cell Diagnostic	Cat: #315631-C3
Recombinant DNA		
pCaggs- *KRAS*^{G12D} (human)	Laboratory of Dr. Lars Zender	N/A
SB13	Laboratory of Dr. Lars Zender	N/A
CRISPR/Cas9 sg-p19 (pX330-sg-p19)	Laboratory of Dr. Lars Zender	N/A
pT3-EF1α-HA-myr-Akt (mouse)	Laboratory of Dr. Xin Chen	RRID: Addgene_31789
pT3-EF1α-YAPS127A (human)	Laboratory of Dr. Xin Chen	RRID: Addgene_86497
pT3-EF1a-HA-FBXW7ΔF (human)	Laboratory of Dr. Xin Chen; Wang et al.; J Hepatol, 2019. PMID: 31195063	N/A
pT3-EF1α-NICD1 (mouse)	Laboratory of Dr. Xin Chen	RRID: Addgene_46047
pT3-CK19-GFP	Laboratory of Dr. Xin Chen; this paper	N/A
Software and algorithms		
Cell Ranger version v3.1.0	10x Genomics	https://support.10xgenomics.com/single-cell-gene-expression/software/downloads/latest
Scanpy v1.4.6	Fabian J. Theis lab, Genome Biology 2018	https://scanpy.readthedocs.io/en/stable
PanglaoDB	Franzén *et al*; Database, Volume 2019, 2019, baz046	https://www.panglaodb.se
g:Profiler (version e99_eg46_p14_f929183)	Raudvere et al; Nucleic Acids Res 2019	https://biit.cs.ut.ee/gprofiler/gost
CellPhoneDB v.2.0.0	Vento-Tormo et al; Nature, 2018. PMID: 30429548	https://www.cellphonedb.org
R v3.5.0	The R Project for Statistical Computing	https://www.r-project.org
Python v3.7.4	Python Software Foundation	https://www.python.org
IBM SPSS version 24	IBM	http://www.ibm.com
GraphPad Prism v.8.0	GraphPad Software	https://www.graphpad.com
Fiji ImageJ v2.0.0-rc-69/1.52p	Image J	https://imagej.net/Fiji
FlowJo (v10.6.2)	N/A	www.flowjo.com
BioRender	©BioRender	biorender.com
QuPath v.0.1.3	Queen's University, Belfast, Northern Ireland	https://qupath.github.io
LEICA Digital Image Hub 4.0 image server	Leica	N/A
Other		
gentleMACS Octo Dissociator	Miltenyi Biotec	Cat: #130-095-937
NovaSeq 6000 Sequencing System	Illumina	N/A
Nano-Zoomer Digital Pathology scanner	Hamamatsu, Japan	N/A
Slide scanner	Leica	Cat: # SCN400

REAGENT or RESOURCE	SOURCE	IDENTIFIER
Bioanalyzer 2100	Agilent Technologies	Model G2939B